REDUCED-ORDER MODELING OF BLADED DISK SYSTEMS WITH SHROUDS BY COMPONENT MODE SYNTHESIS

A THESIS SUBMITTED TO
THE GRADUATE SCHOOL OF NATURAL AND APPLIED SCIENCES
OF
MIDDLE EAST TECHNICAL UNIVERSITY

BY

EHSAN NAGHIZADEH

IN PARTIAL FULFILLMENT OF THE REQUIREMENTS
FOR
THE DEGREE OF MASTER OF SCIENCE
IN
MECHANICAL ENGINEERING

JUNE 2022

Approval of the thesis:

REDUCED-ORDER MODELING OF BLADED DISK SYSTEMS WITH SHROUDS BY COMPONENT MODE SYNTHESIS

submitted by **EHSAN NAGHIZADEH** in partial fulfillment of the requirements for the degree of **Master of Science in Mechanical Engineering, Middle East Technical University** by,

Prof. Dr. Halil Kalıpçılar
Dean, Graduate School of **Natural and Applied Sciences**

Prof. Dr. M. A. Sahir Arıkan
Head of the Department, **Mechanical Engineering**

Prof. Dr. Ender Ciğeroğlu
Supervisor, **Mechanical Eng. Dept., METU**

Examining Committee Members:

Prof. Dr. Yiğit Yazıcıoğlu
Mechanical Engineering Dept., METU

Prof. Dr. Ender Ciğeroğlu
Mechanical Engineering Dept., METU

Assoc. Prof. Dr. Mehmet Bülent Özer
Mechanical Engineering Dept., METU

Assist. Prof. Dr. Gökhan Özgen
Mechanical Engineering Dept., METU

Assist. Prof. Dr. Selçuk Himmetoğlu
Mechanical Engineering Dept., Hacettepe University

Date: 03.06.2022

I hereby declare that all information in this document has been obtained and presented in accordance with academic rules and ethical conduct. I also declare that, as required by these rules and conduct, I have fully cited and referenced all material and results that are not original to this work.

Name Last name : Ehsan Naghizadeh

Signature :

ABSTRACT

REDUCED-ORDER MODELING OF BLADED DISK SYSTEMS WITH SHROUDS BY COMPONENT MODE SYNTHESIS

Naghizadeh, Ehsan
Master of Science, Mechanical Engineering
Supervisor: Prof. Dr. Ender Ciğeroğlu

June 2022, 96 pages

High computation costs imposed by a large number of degrees of freedom hamper the vibration analysis for blade disk systems. Moreover, mistuning, which necessitates the solution of the problem numerous times, and contact surfaces which require displacement data on shroud Degrees of Freedom (DOFs) with high accuracy, highlight the demand for an efficient reduced-order model. Consequently, aiming at deriving results with acceptable accuracy while minimizing computational cost, researchers have proposed different reduction techniques. In this context, Component Mode Synthesis (CMS) methods that follow the famous divide and conquer theory are approved to be very effective. In this study, first, the most famous reduction techniques based on CMS, namely, Rubin, Hurty/Craig-Bampton, Dual Craig-Bampton, and Mixed interface methods, are implemented for reducing the computational cost of an academic bladed disk system with shrouds. A new reduction method is proposed by capitalizing on the information derived from the proceeding comparison study, which is a generalized case for Rubin and Hurty/Craig-Bampton methods. Subsequently, the efficiency of the proposed method is compared with its rivals available in the literature in both tuned and mistuned case studies. It is concluded that the proposed method can provide superior accuracy while maintaining a relatively low computational cost when appropriately used with the cyclic symmetry property and Rubin method for a tuned bladed disk system. For the mistuned case, the reduction of the blade sector is analogous to the tuned case. Therefore, special attention is paid to the disk assembly for the mistuned case. Three different reduction approaches are proposed for the disk segment. Moreover, an interface reduction method is implemented to reduce the size of the model further. Finally, each of these methods is implemented on the disk sector and coupled with the reduced blade segment to create a reduced-order model of the entire bladed disk assembly. The Reduced Order Model (ROM) performance is investigated for different mistuning patterns. It is concluded that the reduction measure proposed in this work can bring excellent results and drastically reduce the computational time for the analysis of mistuned bladed disk.

Keywords: Reduced-Order Modeling, Component Mode Synthesis (CMS), Bladed Disk Systems, Mistuning, Shrouds

ÖZ

BİLEŞEN BİÇİM SENTEZİ İLE ÇIKINTI TİP SÖNÜMLEYİCİLİ KANATÇIKLI DİSK SİSTEMLERİNİN İNDİRGENMİŞ MODELLİNİN OLUŞTURULMASI

Naghizadeh, Ehsan
Yüksek Lisans, Makina Mühendisliği
Tez Yöneticisi: Prof. Dr. Ender Ciğeroğlu

Haziran 2022, 96 sayfa

Çok sayıda serbestlik derecesinin getirdiği yüksek hesaplama maliyetleri, kanatçıklı disk sistemleri için titreşim analizini engeller. Ayrıca, problemin defalarca çözülmesini içeren yanlış ayarlama ve örtü DOF'lerinde yüksek doğrulukla yer değiştirme verileri gerektiren doğrusal olmayan temas yüzeyleri, verimli bir azaltılmış indirgenmiş modeli talebini vurgulamaktadır. Sonuç olarak, hesaplama maliyetini en aza indirirken kabul edilebilir doğrulukta sonuçlar elde etmeyi amaçlayan araştırmacılar, farklı indirgeme teknikleri önermişlerdir. Bu bağlamda, ünlü böl ve yönet teorisini takip eden bileşen biçim sentez yöntemlerinin çok etkili olduğu onaylanmıştır. Bu çalışmada, ilk olarak, bileşen biçim sentez kurulmuş en ünlü indirgeme teknikleri, yani Rubin, Hurty/Craig-Bampton, Dual Craig-Bampton ve Karışık arayüz yöntemleri, örtülü akademik bir kanatçıklı disk sisteminin hesaplama maliyetini azaltmak için uygulanmıştır. Rubin ve Hurty/Craig-Bampton yöntemleri için genelleştirilmiş bir durum olan devam eden karşılaştırma çalışmasından elde edilen bilgilerden yararlanılarak yeni bir indirgeme düzeni önerilmiştir. Daha sonra önerilen yöntemin etkinliği, hem düzenli hem de düzensiz ayarlı durum çalışmalarında rakipleriyle karşılaştırılmıştır. Önerilen yöntemin, düzenli kanatçıklı disk sistemi için döngüsel simetri özelliği ve Rubin yöntemi ile uygun şekilde kullanıldığında nispeten düşük bir hesaplama maliyetini korurken üstün doğruluk sağlayabildiği sonucuna varılmıştır. düzensiz durum için, kanatçıklı sektörünün azalması ayarlı duruma benzer. Bu nedenle, düzensiz durum için disk düzeneğine özel dikkat gösterilir. Disk segmenti için üç farklı indirgeme yaklaşımı önerilmiştir. Ayrıca, modelin boyutunu daha da azaltmak için bir arayüz azaltma yöntemi uygulanmaktadır. Son olarak, bu yöntemlerin her biri disk sektörü üzerinde uygulanır ve tüm kanatçıklı disk düzeneğinin azaltılmış sıralı bir modelini oluşturmak için indirgenmiş kanatçıklı segmenti ile birleştirilir. indirgenmiş Modeli performansı, farklı düzensiz ayarlama modelleri için araştırılır. Bu çalışmada önerilen indirgen önleminin mükemmel sonuçlar getirebileceği ve düzensiz ayarlanmış kanatçıklı disk için hesaplama süresini önemli ölçüde azaltabileceği sonucuna varılmıştır.

Anahtar Kelimeler: İndirgenmiş Modelleme, Bileşen Biçim Sentezi, Kanatçıklı Disk Sistemleri, Düzensizlik, Örtüler

To my family and all the beloved ones,

ACKNOWLEDGMENTS

The author wishes to express his deepest gratitude to his supervisor Prof. Dr. Ender Ciğeroğlu for his guidance, advice, criticism, encouragements and insight throughout the research.

TABLE OF CONTENTS

CHAPTERS

LIST OF TABLES

TABLES

LIST OF FIGURES

FIGURES

LIST OF ABBREVIATIONS

ABBREVIATIONS	
CB	Craig-Bampton
CMS	Component Mode Synthesis
DCB	Dual Craig-Bampton
DOF	Degree of Freedomn
EVP	Eigenvalue Problem
FEM	Finite Element Method
FRF	Frequency Response Function
HB	Harwell-Boing
HCF	High Cyclic Fatigue
MAC	Modal Assurance Criterion
MMXD	Modified Mixed Interface
MXD	Mixed Interface
SNM	Subset of Nominal Modes

CHAPTER 1

INTRODUCTION

The first chapter briefly introduces the vibration analysis for the bladed disk systems along with the problems hampering the way. Subsequently, possible methodologies to tacked the problems are reviewed. Finally, a description of the following chapters of the thesis is provided.

1.1 Vibration Analysis for Bladed Disk Systems

The design of bladed disk systems is a challenging task for engineers due to the harsh working conditions and various types of static and dynamic forces in their operating environment. Bladed disk systems typically suffer from high cyclic fatigue failure (HCF) caused by large deformation concentrated on some blades [1]. From the strategies to tackle the energy concentration on blades, the approach to dissipate this unwanted energy through friction has been widely used in industry. Different types of friction contact elements have been introduced to the literature, i.e., shrouds, contact between blade-to-disk interface, under-platform dampers, ring dampers, and wedge dampers. The problem of making a balance between the safety and efficiency of the bladed disks is an ongoing topic of research among scientists. A sophisticated understanding of the physics of bladed disk components and forces applied to them in their working condition is the first step toward finding a solution.

Numerical investigation of the bladed disk systems is a tedious task. Due to their elaborate geometry, a fine mesh is required to predict their behavior accurately, so they usually are represented by enormous FEM models. In addition, a statistical investigation may be required due to the mistuning phenomenon [2]. That is to solve the problem millions of times to gather the required information to account for the random nature of the mistuning patterns. In addition, the presence of nonlinear elements in the model obligates a precise prediction of the displacements for the contact elements [3]. In order to alleviate the high computational cost imposed by the circumstances mentioned above and simultaneously provide accurate results, researchers have introduced reduced-order modeling techniques. These methods aim to facilitate the act of deriving the vibration characteristics of the structure. They accelerate the investigation process and allow the scientist to conduct parametric analyses, which are invaluable in the design stage.

1.2 CMS Methods

The computational burden of the analysis can be alleviated by several methods, one of which is the dynamic substructuring or Component Mode Synthesis (CMS). As the name implies, the primary procedure in this technique is analogous to the famous divide and conquer approach [4]. That is to reduce a large system by dividing it into its components, and after reducing the size of each component, reassemble them again to reach the reference structure. After the reduction procedure, the final degrees of freedom will be some generalized coordinates on each component, interfaced DOFs, and DOFs of which physical information, like displacement or force, is required. The Component-Mode Synthesis (CMS) methods have been known to be very useful in dealing with extensive finite element problems [5].

Although they are similar in the main procedure, reduction techniques based on substructuring, or CMS, fall into different categories regarding how they describe each substructure's interface. According to these criteria, two distinct methodologies are introduced, namely: fixed-interface methods and free-interface methods. A combination of dynamic and static modes composes the reduction basis for these methods. While the interface DOFs are held fixed in calculating the vibration modes in the fixed-interface methods [6], they are left free in the derivation of the vibration modes in the free-interface methods [7]. The static modes of each method are derived accordingly, i.e., static constraint modes for fixed-interface methods and flexibility modes for the free-interface method [8]. A detailed description of all the static and dynamic modes used in the reduction basis is presented in the proceeding sections.

Reduction techniques based on substructuring have long been introduced to the literature. The advent of dynamic substructuring or component-mode synthesis (CMS) can be traced back to the mid-1960s when Hurty [9] introduced a reduction technique based on fixed-interface modes. The proceeding paper by Craig and Bampton [10] was the cornerstone in the development of the CMS methods. Their work, which indeed was originated by Hurty, further popularized the fixed-interface reduction technique in the world of dynamic substructuring. For the following years, CMS methods attracted the attention of scientists. As an alternative to the fixed-interface method, several scientists explored the free-interface methods, which culminated in the introduction of MacNeal [11], Rubin [7], and Hintz [12] methods. A detailed review of the works done in the 20th century can be found in [13]. Both fixed and free-interface approaches have their advantages and disadvantages, highlighting the question, "Which method servers best for a specific geometry?"

In 1982, Irretier first implemented the CMS methods for analyzing mistuned bladed disk systems [14]. Later Chun et al. [15] used CMS methods to investigate the vibration of blisks mounted on a flexible rotor. Reduced-order modeling of the bladed disk with shrouds was introduced by Bladh et al. [16]. They further published a two-parted paper on the theoretical background and application of the CMS method for mistuned blade disk systems [17], [18]. CMS method subsequently expanded to mitigate the high computational cost stemming from the nonlinearities introduced mainly by contact frictions. In recent years, researchers have explored different characteristics of the CMS methods to build an efficient reduction basis for bladed disk systems. A comparative study by Mashayekhi et al. [19], [20] examined the most recent reduction techniques and their efficiency. They also came up with a hybrid technique for a mistuned bladed disk with friction contact [21]. By considering the blade-disk interaction, Pourkiaee and Zucca proposed a method to reduce the size of a bladed disk with shrouds [22][23][24]. They took advantage of the Loaded Interface (LI) modes shapes [25] to further reduce the size of interface DOFs. In [26], Yuan et al. proposed an adaptive reduction method. Quaegebeur et al. [27][28] introduced a novel two-stage reduction that implements the cyclic symmetric property.

1.3 Thesis Statement and Chapter Review

Despite the extensive research conducted on the reduced-order modeling of the bladed disk systems with shrouds, the need for an efficient ROM capable of reducing the size of the problem and paving the way for parametric analysis and, at the same time providing accurate predictions of the displacements at shrouds DOFs is still persisting. Thus, this thesis is dedicated to developing an efficient ROM for the specific geometry of bladed disk systems with shrouds that can bring the characteristics required.

An outline of the following chapters is presented as follows.

Chapter two represents the fundamental methodologies required for the reduced-order modeling of the bladed disk systems and modal analysis of cyclic structures. The chapter is composed of a comprehensive formulation of the real and complex form of cyclic symmetry with a brief mode shape interpretation. Subsequently, reduction techniques based on Component Mode Synthesis (CMS) are formulated. In this section, a new mixed interface reduction technique is proposed. The proposed method is the fruit of the novel perspective on the modal contribution of the substructures to the final vibration state of the bladed disk system. Furthermore, an enhanced interface reduction method is formulated to expand the compatibility of the current interface reduction method with both free and fixed interface reduction techniques. Finally, mistuning modeling is given. The last section answers the question of how mistuning is projected on different blades when reduction is applied to the system.

In chapter three, case studies to implement different reduction methods are given. In order to validate the reduction methods, an elaborate finite element model is created. Chapter three describes the model and introduces the tuned and mistuned bladed disk systems.

Almost all of the reduction methods based on component modes synthesis are included in this study. Moreover, a compatible combination of the CMS methods and cyclic symmetry analysis is implemented for both tuned and mistuned cases. The results of the methods are given in chapter four. Besides, a discussion and assessment of the efficiency of the methods are provided in this chapter.

Eventually, chapter five concludes all the results and findings in the previous chapters.

CHAPTER 2

METHODOLOGY

Reduced-order modeling of bladed disk systems can become arduous due to large finite element models and numerous components. Thus, it is necessary to implement a combination of different reduction techniques since neither single one of the methods can bring sufficiently reduced models. In particular, when mistuning exists, it is desirable to use cyclic symmetry property compatible with the problem's hypothesis. This chapter discusses the fundamentals of mathematical models and reduction procedures required for the reduced-order modeling of bladed disk systems. It should be noted that cyclic symmetry is included in this chapter since it is used as means of model reduction.

This chapter starts by exploring the cyclic symmetry property, which is vital for the vibration analysis of turbomachinery. Both real and complex formulation of the cyclic symmetry analysis is given, along with a brief subsection about mode anticipation for real and complex cyclic formulation. Subsequently, reduction methods are investigated based on Component Mode Synthesis (CMS). First, a definition of different dynamic and static modes is given. The mentioned modes are the main ingredients of the reduction basis. Next, conventional fixed and free interface methods are described. Notably, the well-known Craig-Bampton (CB) method is included in this study from fixed interface methods. The powerful Rubin and Dual Craig-Bampton (DCB) methods are selected from the free interface methods. In addition to the conventional methods, a more recent technique, called the mixed-interface method (MXD), which is a generalization of Craig-Bampton, and Dual Craig-Bampton methods, are also formulated.

One of the original contributions of this work is to introduce a Modified Mixed interface Method (MMXD) to the specific geometry of the bladed disk systems. The method is a generalization of the Rubin and Craig-Bampton method.

Chapter two introduces interface reduction methods. The interface reduction becomes especially important in reducing the disk sector when the disk to disk interface possesses a large number of DOFs.

Finally, the last section gives instructions on the modeling of the mistuning. The mistuning in this study and most of the literature is considered on the blade sector only.

2.1 Cyclic Symmetry

Cyclic symmetry property is a well-known concept in turbomachinery. Extensive research has been dedicated to the analysis of the cyclic symmetric structures. Moreover, commercial finite elements software guidelines like MSC/NASTRAN [29] on the vibration analysis of the cyclic symmetric analysis. However, the cyclic symmetry plays such a prominent role in the reduced-order modeling of the bladed disk systems that a brief review of the concept is desirable [30]–[34].

2.1.1 Fundamental Concepts

In this subsection, the fundamental concepts of the cyclic symmetry analysis are given. The concepts of interest are Kronecker Product, coordinate transformation in cylindrical framework, Circulant Matrices, Fourier Matrices, and Engine Order Excitation.

Kronecker Product

Kronecker product is a unique multiplication technique that facilitates the multiplication of large matrices and eliminates the need for a for loop in the algorithms. Throughout this thesis, the Kronecker product is shown with ⊗ symbol.

In order to illustrate the multiplication scheme by the Kronecker operator, let us assume $\mathbf{A}$, and $\mathbf{B}$, to be two matrices of arbitrary size, then

$$\mathbf{A} \otimes \mathbf{B} = \begin{bmatrix} \mathbf{A}_{11}\mathbf{B} & \mathbf{A}_{12}\mathbf{B} & \dots \\ \mathbf{A}_{21}\mathbf{B} & \mathbf{A}_{22}\mathbf{B} & \dots \\ \vdots & \vdots & \ddots \end{bmatrix} \qquad 2.1$$

Some essential characteristics of the Kronecker products are as follows:

- The multiplication is not invertible

$$\mathbf{A} \otimes \mathbf{B} \neq \mathbf{B} \otimes \mathbf{A} \qquad 2.2$$

- A scaler is distributive into the product

$$c(\mathbf{A} \otimes \mathbf{B}) = (c\mathbf{A}) \otimes \mathbf{B} = \mathbf{A} \otimes (c\mathbf{B}) \qquad 2.3$$

- Associative

$$\mathbf{C} \otimes (\mathbf{A} \otimes \mathbf{B}) = (\mathbf{C} \otimes \mathbf{A}) \otimes \mathbf{B} \qquad 2.4$$

- If both $\mathbf{A}$, and $\mathbf{B}$ are invertible

$$(\mathbf{A} \otimes \mathbf{B})^{-1} = \mathbf{A}^{-1} \otimes \mathbf{B}^{-1} \qquad 2.5$$

$$(\mathbf{A} \otimes \mathbf{B})' = \mathbf{A}' \otimes \mathbf{B}' \qquad 2.6$$

Transformation in the Cylindrical Framework

one fundamental transformation that can be considered a prerequisite for the cyclic analysis is the transformation of the dependent DOFs of the right neighbor of the fundamental sector to the coordinates system of the fundamental sector. If we consider our system to be rotationally periodic along the z-axis, then the mentioned transformation can be done according to the following formulation.

$$\mathbf{T}_c = \begin{bmatrix} \cos\theta & -\sin\theta & 0 \\ \sin\theta & \cos\theta & 0 \\ 0 & 0 & 1 \end{bmatrix} \qquad 2.7$$

$\mathbf{T}_c$ is the transformation matrix for a point on the Cartesian framework, which rotates the point on the x-y plane and around the z-axis for θ rad. In the cyclic analysis, the θ angle is referred to as the inter-blade phase angle or inter-blade angle.

$$\theta = (2\pi)/N \qquad 2.8$$

Where N is the total number of blades in the bladed disk assembly. In order to transform all the dependent DOFs on the right neighbor of the fundamental sector, the Kronecker product is used. The procedure starts by first partitioning the coordinates into the dependent, independent, and normal coordinates, as illustrated below.

$$\mathbf{x} = \begin{Bmatrix} \mathbf{x}_\alpha \\ \mathbf{x}_\beta \\ \mathbf{x}_n \end{Bmatrix} \qquad 2.9$$

In the above equation, β denotes the dependent DOFs, α represents the independent DOFs, and all other DOFs are in the n subscript. The dependent DOFs can be transformed into the new coordinate system by rotating them around the z-axis.

$$\bar{\mathbf{x}}_\beta = \mathbf{T}_\beta \mathbf{x}_\beta \qquad 2.10$$

In the above equation, $\bar{\mathbf{x}}_\beta$ are the transformed dependant DOFs in the fundamental coordinate system. The overall transformation matrix will take the form

$$\bar{\mathbf{x}} = \mathbf{T}\mathbf{x} \qquad 2.11$$

the **T** matrix is the total transformation matrix on which one may project the mass and stiffness matrices.

$$\mathbf{T} = \begin{bmatrix} \mathbf{I}_\alpha & 0 & 0 \\ 0 & \mathbf{T}_\beta & 0 \\ 0 & 0 & \mathbf{I}_n \end{bmatrix} \qquad 2.12$$

The projection of the mass and stiffness matrices onto the transformation matrix are as follows

$$\bar{\mathbf{k}} = \mathbf{T}'\mathbf{k}\mathbf{T} \tag{2.13}$$

And the transformation of the mass matrix is exactly the same.

One critical issue that may occur, which is very confusing, is that this vital transformation becomes redundant on some special occasions—this occurs in dealing with finite element data. As usually, for validation purposes, one wishes to perform cyclic symmetry on a commercial finite element model and do the same from the cyclic formulation. Mass and stiffness matrices are obtained from the finite element software in such situations. Suppose a cyclic analysis is carried out on the finite element software prior to the extraction of the element matrices. In that case, the transformation mentioned above is automatically imposed on the extracted matrices. Even after turning off the cyclic option, the matrices derived from the software are already transformed, and a repetition of this transformation gives wrong results.

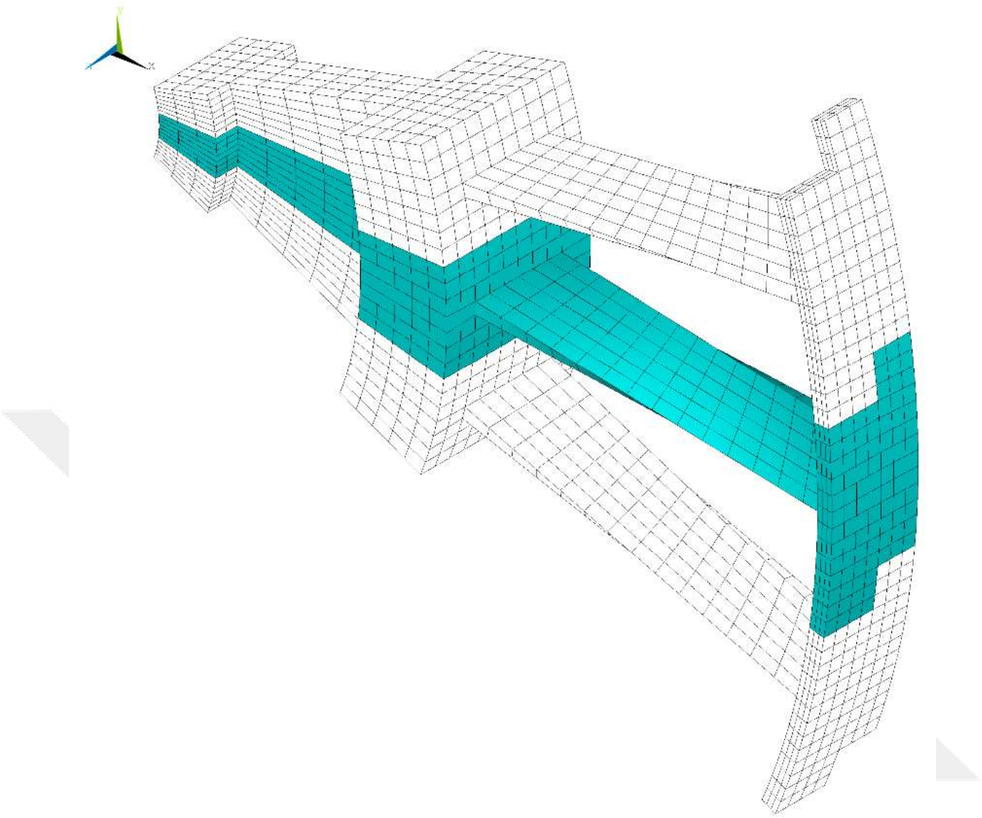

Figure 2.1. Rotation of the fundamental sector around the z-axis to make the left and right neighbor sectors

Circulant Matrices

Circulant matrices are encountered in many disciplines [35], one of which is the structural analysis of the cyclically symmetric structures. This happens because the cyclic structure can be assumed as a chain of lumped mass and stiffness where the last mass is also coupled with the first one. This unique symmetry builds matrices of the shape below

$$\mathbf{CM} = \begin{bmatrix} M_1 & M_2 & \dots & M_N \\ M_N & M_1 & \dots & M_{N-1} \\ \vdots & \vdots & \ddots & \vdots \\ M_2 & M_3 & \dots & M_1 \end{bmatrix} \qquad 2.14$$

As it can be understood from the above expression, the circulant matrix is created by moving a set of N scalers along the rows. The N by N **CM** matrix can be built out of a set of scaler values $M = \{M_i, i = 1, 2, \dots N\}$

For the case of lumped parameter modeling, it can be shown easily that the mass and stiffness matrices will take the form

$$\mathbf{K} = \begin{bmatrix} 2k & -k & \dots & -k \\ -k & 2k & \dots & 0 \\ \vdots & \vdots & \ddots & \vdots \\ -k & 0 & \dots & 2k \end{bmatrix}, \quad \mathbf{M} = \begin{bmatrix} m & 0 & \dots & 0 \\ 0 & m & \dots & 0 \\ \vdots & \vdots & \ddots & \vdots \\ 0 & 0 & \dots & m \end{bmatrix} \qquad 2.15$$

However, for the case of finite element models, the concept of circulant matrices is extended to block circulant matrices

$$\mathbf{CM} = \begin{bmatrix} \mathbf{M}_1 & \mathbf{M}_2 & \dots & \mathbf{M}_N \\ \mathbf{M}_N & \mathbf{M}_1 & \dots & \mathbf{M}_{N-1} \\ \vdots & \vdots & \ddots & \vdots \\ \mathbf{M}_2 & \mathbf{M}_3 & \dots & \mathbf{M}_1 \end{bmatrix} \qquad 2.16$$

In contrast to the circulant matrix built from the scaler values, in the block diagonal form, the generating elements are matrices of size $m \times m$. Consequently, the product of the block circulant matrix is a Nm by Nm matrix where its elements are the matrices of size m.

For the case of bladed disk systems, if each sector's mass and stiffness matrices are presented in its local coordinate system, the resulting matrices will be in the shape of a circulant matrix. The mentioned notion is of especial importance for two reasons: being in the shape of a circulant matrix is very advantageous sine Fourier matrices can easily diagonalize circulant matrices. Second, the matrix will take the circulant form only when all the sectors are described in their local coordinate systems. The latter is essential to note later in the back transformation of the cyclic coordinates to physical coordinates.

Fourier Matrices

As asserted in the previous section, circulant matrices can be diagonalized using Fourier matrices [33]. It is vital to diagonalize the circulant matrices corresponding to the bladed disk systems. Diagonalization provides the possibility to break down the large element matrices into several (equal to the number of harmonic indices) smaller matrices.

There are real and complex forms of the Fourier used for the real and complex formulation of the cyclic symmetry correspondingly. Both formulations are given below.

$$\mathbf{E}^{C}_{m,n} = \frac{1}{\sqrt{N}} e^{i\theta(m-1)(n-1)}, \quad m, n = \{1, 2, \dots, N\} \qquad 2.17$$

In the above equation $i = \sqrt{-1}$, $\theta = 2\pi/N$, and m and n are the row and column indices, respectively.

The real form of the Fourier matrix introduces the concept of single and double harmonies. Although their complex counterpart, real and complex harmonies, have almost equivalent properties, they do not interfere with the calculation of the complex form. As a result, the implementation of the complex formulation is more convenient. The downside of using the complex form is dealing with complex matrices. Nevertheless, for the case of the real formulation, the formulation needs to be applied on single and double harmonics separately. Thus, the formulation and coding process is a bit more cumbersome for the real form of the cyclic formulation.

The definition of the single and double harmonies finds their origin in the vibration pattern of the cyclic symmetry analysis. Single harmonies refer to the vibration pattern at which all the blades vibrate in the same phase or precisely in the opposite phase. Since in the case that the bladed disk assembly is composed of an odd number of blades, all the blades cannot vibrate in out of phase mode, for the systems with an odd number of blades, there is only one single harmonic. Consequently, the number and type of the harmonies are as follows

$$p = \{0,1,2,\dots,p_t\}, \qquad p_t = \begin{cases} N/2 & if\ N\ is\ even \\ (N-1)/2 & if\ N\ is\ odd \end{cases} \tag{2.18}$$

p is the set of harmonic indices, and p_t is its maximum value.

$$p_s = \begin{cases} \{0, p_t\} & if\ N\ is\ even \\ \{0\} & if\ N\ is\ odd \end{cases} \tag{2.19}$$

$$p_d = \begin{cases} \{1,2,\dots,p_t-1\} & if\ N\ is\ even \\ \{1,2,\dots,p_t\} & if\ N\ is\ odd \end{cases} \tag{2.20}$$

In the above expression, p_s, and p_d are the set of single and double harmonies.

Now that a description of single and double harmonies is illustrated, the real form of the Fourier matrix can be easily derived as follows

$$\mathbf{E}^R = \left[\mathbf{E}_0^R, \dots, \mathbf{E}_h^{R,c}, \mathbf{E}_h^{R,s}, \dots, \mathbf{E}_p^R\right] \tag{2.21}$$

$$\mathbf{E}_0^R = \frac{1}{\sqrt{2}}\{\mathbf{1}, \mathbf{1}, \dots, \mathbf{1}\}', \qquad \mathbf{E}_N^R = \frac{1}{\sqrt{2}}\{\mathbf{1}, \mathbf{-1}, \mathbf{1}, \mathbf{-1} \dots, \mathbf{-1}\}' \tag{2.22}$$

$$\left(\mathbf{E}_h^{R,c}\right)_j = \frac{1}{\sqrt{2}}\{\cos\left((h-1)(j-1)\theta\right)\}, \qquad \left(\mathbf{E}_h^{R,s}\right)_j = \frac{1}{\sqrt{2}}\{\sin\left((h-1)(j-1)\theta\right)\} \tag{2.23}$$

In the above equation, j is the row indices that take values from 1 to N. It should be noted that the $\mathbf{E}_N^R$ vector exists only in case of N to be even. The matrix illustration of both real and complex form of the Fourier matrices are given below.

$$\mathbf{E}^C = \frac{1}{\sqrt{N}}\begin{bmatrix} 1 & 1 & 1 & 1 \\ 1 & e^{\theta i} & \dots & e^{(N-1)\theta i} \\ \vdots & \vdots & \ddots & \vdots \\ 1 & e^{(N-1)\theta i} & \dots & e^{(N-1)(N-1)\theta i} \end{bmatrix} \tag{2.24}$$

$$\mathbf{E}^R = \sqrt{\frac{2}{N}} \begin{bmatrix} R & \dots & R & R & \dots & R \\ R & \dots & \cos{(h-1)\theta} & \sin{(h-1)\theta} & \dots & -R \\ R & \dots & \cos{(h-1)(2)\theta} & \sin(h-1)\,(2)\theta & \dots & R \\ \vdots & \ddots & \vdots & \vdots & \ddots & \vdots \\ R & \dots & \cos{(h-1)(N-1)\theta} & \sin{(h-1)(N-1)\theta} & \dots & -R \end{bmatrix} \qquad 2.25$$

In the real formulation expression, h is the harmonic index number which also corresponds to the column index of the matrix, and $R = \frac{1}{\sqrt{2}}$.

When circulant matrices are projected on the Fourier matrices, diagonal or block-diagonal matrices are obtained.

$$\mathbf{C}^C = (\mathbf{E}^C)'\,\mathbf{CM}\,\mathbf{E}^C = \begin{bmatrix} \mathbf{C}_1 & \mathbf{0} & \dots & \mathbf{0} \\ \mathbf{0} & \mathbf{C}_2 & \dots & \mathbf{0} \\ \vdots & \vdots & \ddots & \vdots \\ \mathbf{0} & \mathbf{0} & \dots & \mathbf{C}_N \end{bmatrix} \qquad 2.26$$

For single harmonic indices (p_s) as described earlier the $\mathbf{C}_{p_s}$ elements in the above equation will be real-valued. For the double harmonic indices, on the other hand, $\mathbf{C}_{p_d}$ will be complex.

For the real case:

$$\mathbf{C}^R = (\mathbf{E}^R)'\,\mathbf{CM}\,\mathbf{E}^R = \begin{bmatrix} \mathbf{C}_1 & \mathbf{0} & \dots & \mathbf{0} \\ \mathbf{0} & \mathbf{C}_2 & \dots & \mathbf{0} \\ \vdots & \vdots & \ddots & \vdots \\ \mathbf{0} & \mathbf{0} & \dots & \mathbf{C}_{p_t} \end{bmatrix} \qquad 2.27$$

Where,

$$\mathbf{C}_i = \begin{cases} \mathbf{C}_i & for\ i \in p_s \\ \begin{bmatrix} \mathbf{C}_i^0 & \mathbf{C}_i^1 \\ (\mathbf{C}_i^1)' & \mathbf{C}_i^0 \end{bmatrix} & for\ i \in p_d \end{cases} \qquad 2.28$$

2.1.2 Real Form of Cyclic Symmetry Formulation

In order to apply cyclic symmetry on the bladed disk system, the mass and stiffness matrices of the fundamental sector are extracted from the commercial finite element software. Next, according to the equation sort information, the coordinates are reordered in the following format.

$$\mathbf{x} = \begin{Bmatrix} \mathbf{x}_{\alpha} \\ \mathbf{x}_{\beta} \\ \mathbf{x}_{n} \end{Bmatrix}, \qquad \mathbf{k} = \begin{bmatrix} \mathbf{k}_{\alpha\alpha} & \mathbf{k}_{\alpha\beta} & \mathbf{k}_{\alpha n} \\ \mathbf{k}_{\beta\alpha} & \mathbf{k}_{\beta\beta} & \mathbf{k}_{\beta n} \\ \mathbf{k}_{n\alpha} & \mathbf{k}_{n\beta} & \mathbf{k}_{nn} \end{bmatrix} \qquad 2.29$$

The formulation is the same for the mass matrix unless otherwise mentioned.

As mentioned previously, a vital rotation is needed for the dependent coordinates to be transformed into the independent coordinates.

$$\bar{\mathbf{x}} = \mathbf{T} \begin{Bmatrix} \mathbf{x}_{\alpha} \\ \mathbf{x}_{\beta} \\ \mathbf{x}_{n} \end{Bmatrix}, \qquad \bar{\mathbf{k}} = \mathbf{T}' \begin{bmatrix} \mathbf{k}_{\alpha\alpha} & \mathbf{k}_{\alpha\beta} & \mathbf{k}_{\alpha n} \\ \mathbf{k}_{\beta\alpha} & \mathbf{k}_{\beta\beta} & \mathbf{k}_{\beta n} \\ \mathbf{k}_{n\alpha} & \mathbf{k}_{n\beta} & \mathbf{k}_{nn} \end{bmatrix} \mathbf{T} \qquad 2.30$$

After the rotation, the element matrices are ready to be coupled for each harmonic index. The coupling procedure will follow the conventional approach of satisfying the compatibility condition of the cyclic interfaces. The critical issue here is to consider double matrices for the double harmonies. Consequently, the element matrices can be obtained as follows.

$$\tilde{\mathbf{k}}_h = \begin{cases} \bar{\mathbf{k}} & for\ h \in p_s \\ \begin{bmatrix} \bar{\mathbf{k}} & \mathbf{0} \\ \mathbf{0} & \bar{\mathbf{k}} \end{bmatrix} & for\ \ h \in p_d \end{cases} \qquad 2.31$$

$$\tilde{\mathbf{x}}_h = \begin{cases} \{\mathbf{x}_{\alpha} \quad \bar{\mathbf{x}}_{\beta} \quad \mathbf{x}_{n}\}' & for\ h \in p_s \\ \{\mathbf{x}_{\alpha}^{c} \quad \bar{\mathbf{x}}_{\beta}^{c} \quad \mathbf{x}_{n}^{c} \quad \mathbf{x}_{\alpha}^{s} \quad \bar{\mathbf{x}}_{\beta}^{s} \quad \mathbf{x}_{n}^{s}\}' & for\ h \in p_d \end{cases} \qquad 2.32$$

in the above equation $\tilde{\mathbf{k}}_h$ are the element matrix representation required for the coupling process. The ~ symbol is used to distinguish the matrices before and after the coupling process and to avoid any misunderstanding. The compatibility equations can be written.

For single harmonies, i.e., $h \in p_s$

$$\bar{\mathbf{x}}_\beta = cos(\phi_h)\mathbf{x}_\alpha + sin(\phi_h)\mathbf{x}_\alpha \qquad 2.33$$

And for the double harmonies, i.e., $for\ h \in p_d$

$$\begin{aligned} \bar{\mathbf{x}}_\beta^c &= cos(\phi_h)\mathbf{x}_\alpha^c + \sin(\phi_h)\,\mathbf{x}_\alpha^s \\ \bar{\mathbf{x}}_\beta^s &= cos(\phi_h)\mathbf{x}_\alpha^s - \sin(\phi_h)\,\mathbf{x}_\alpha^c \end{aligned} \qquad 2.34$$

In the above equations, ϕ_h is the phase angle corresponding to the harmonic number (h).

The coupling procedure for the single and double harmonies can be conducted through matrix multiplication.

For single harmonies, i.e., $h \in p_s$

$$\tilde{\mathbf{x}}_h = \begin{Bmatrix} \mathbf{x}_\alpha \\ \bar{\mathbf{x}}_\beta \\ \mathbf{x}_n \end{Bmatrix} = \begin{bmatrix} \mathbf{I}_\alpha & \mathbf{0} \\ \mathbf{I}_\alpha cos(\phi_h) & \mathbf{0} \\ \mathbf{0} & \mathbf{I}_n \end{bmatrix} \begin{Bmatrix} \mathbf{x}_\alpha \\ \mathbf{x}_n \end{Bmatrix} = \mathbf{T}_S^{cyc}\mathbf{x}_h \qquad 2.35$$

And for double harmonies, i.e., $h \in p_d$

$$\begin{aligned} \tilde{\mathbf{x}}_h = \begin{Bmatrix} \mathbf{x}_\alpha^c \\ \bar{\mathbf{x}}_\beta^c \\ \mathbf{x}_n^c \\ \mathbf{x}_\alpha^s \\ \bar{\mathbf{x}}_\beta^s \\ \mathbf{x}_n^s \end{Bmatrix} &= \begin{bmatrix} \mathbf{I}_\alpha & \mathbf{0} & \mathbf{0} & \mathbf{0} \\ \mathbf{I}_\alpha cos(\phi_h) & \mathbf{0} & \mathbf{I}_\alpha \sin(\phi_h) & \mathbf{0} \\ \mathbf{0} & \mathbf{I}_n & \mathbf{0} & \mathbf{0} \\ \mathbf{0} & \mathbf{0} & \mathbf{I}_\alpha cos(\phi_h) & \mathbf{0} \\ -\mathbf{I}_\alpha \sin(\phi_h) & \mathbf{0} & \mathbf{I}_\alpha & \mathbf{0} \\ \mathbf{0} & \mathbf{0} & \mathbf{0} & \mathbf{I}_n \end{bmatrix} \begin{Bmatrix} \mathbf{x}_\alpha^c \\ \mathbf{x}_n^c \\ \mathbf{x}_\alpha^s \\ \mathbf{x}_n^s \end{Bmatrix} \\ &= \mathbf{T}_D^{cyc}\mathbf{x}_h \end{aligned} \qquad 2.36$$

After this final coupling process, the mass and stiffness matrices for the coupled system for each harmonic index can be found by projecting the matrices onto the cyclic coupling basis, i.e. $\mathbf{T}_S^{cyc}$, and $\mathbf{T}_D^{cyc}$

$$\begin{aligned} \mathbf{k}_h &= \left(\mathbf{T}_S^{cyc}\right)'\tilde{\mathbf{k}}_h\mathbf{T}_S^{cyc}, \qquad for\ h \in p_s \\ \mathbf{k}_h &= \left(\mathbf{T}_D^{cyc}\right)'\tilde{\mathbf{k}}_h\mathbf{T}_D^{cyc}, \qquad for\ h \in p_d \end{aligned} \tag{2.37}$$

2.1.3 Complex Form of Cyclic Symmetry Formulation

The complex form of the cyclic symmetry formulation is more straightforward than the real form. The coordinate transformation of the dependent and independent DOFs is also required here, and the procedure is the same as the real form. Therefore, the formulation here is based on the matrices derived from Eq. 2.30.

In contrast to the real form, there is no distinction between the single and double harmonies. This facilitates the coding and mathematical representation of the formulation.

$$\tilde{\mathbf{x}}_h = \{\mathbf{x}_\alpha \quad \bar{\mathbf{x}}_\beta \quad \mathbf{x}_n\}' \quad for\ h \in p \tag{2.38}$$

The coupling procedure will take the following form.

$$\bar{\mathbf{x}}_\beta = e^{i\phi_h}\mathbf{x}_\alpha, \qquad for\ h \in p \tag{2.39}$$

It can be understood from the above equation that, depending on the value of the ϕ_hThe resulting coefficient may become a complex number. More precisely, the coefficient for the double harmonies will become complex, while the single harmonic indices will result in a real coefficient.

The coupling procedure can be achieved by the matrix multiplication as follows.

$$\tilde{\mathbf{x}}_h = \begin{Bmatrix} \mathbf{x}_\alpha \\ \bar{\mathbf{x}}_\beta \\ \mathbf{x}_n \end{Bmatrix} = \begin{bmatrix} \mathbf{I}_\alpha & \mathbf{0} \\ \mathbf{I}_\alpha e^{i\phi_h} & \mathbf{0} \\ \mathbf{0} & \mathbf{I}_n \end{bmatrix} \begin{Bmatrix} \mathbf{x}_\alpha \\ \mathbf{x}_n \end{Bmatrix} = \mathbf{T}^{cyc}\mathbf{x}_h \tag{2.40}$$

$$\mathbf{k}_h = (\mathbf{T}^{cyc})'\tilde{\mathbf{k}}_h\mathbf{T}^{cyc}, \qquad for\ h \in p \tag{2.41}$$

It is also worth mentioning that the $'$ is a complex conjugate transpose operator.

2.2 Reduction Based on CMS Methods

In this section, a comprehensive description of the mathematical formulation of the different reduction techniques is provided. Subsequently, the novel modified mixed method (MMXD) is formulated. All the reduction methodologies follow the same reduction pattern. That is to divide the fundamental sector into a blade, and disk components reduce the size of each component and finally assemble them again to reach the fundamental sector. The procedure of coupling sectors to build the entire bladed disk system (which in this model is composed of 26 sectors) is carried out using the cyclic symmetry property Figure 2.1. Thus, the boundary DOFs of the neighbor sectors are not included in the final DOFs.

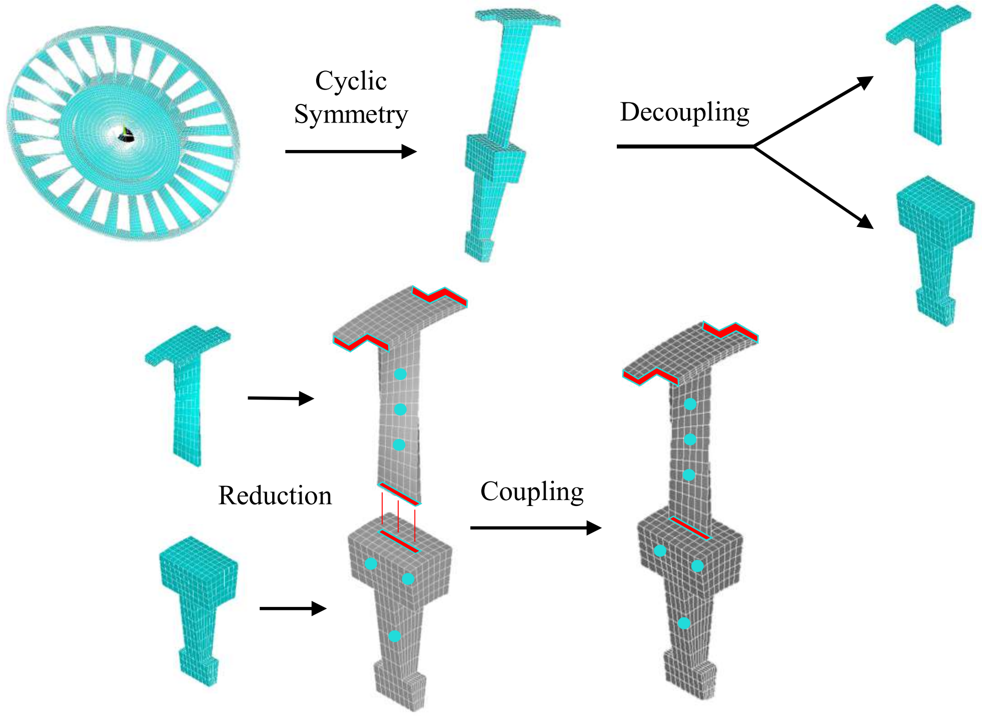

Figure 2.2. Reduction procedure for the tuned bladed disk system

2.2.1 Static and Dynamic Modes Required for the Reduction Basis

Both fixed and free-interface reduction methods use two sets of vectors to approximate the mass and stiffness matrices of a substructure, namely static and dynamic vectors. Static vectors are the static deformation shape of the structure to some external loading. On the other hand, dynamic modes are the vibration modes shapes of the structure. Free-interface reduction methods use attachment modes and free-interface vibration modes, whereas fixed-interface reduction methods use constraint modes and fixed-interface vibration modes.

Static Constraint Modes

Static constraint modes ($\boldsymbol{\Lambda}_c$) are derived by neglecting the dynamic motion of the system. The modes are physically perceived to be the deformation shape of the structure while unit displacement is applied to one of the boundary DOFs, whereas other boundary DOFs are held fixed. The first step in calculating the static constraint modes is dividing the component DOFs into internal (i) and interface or boundary (b)DOFs.

$$\mathbf{u} = \begin{Bmatrix} \mathbf{x}_i \\ \mathbf{x}_b \end{Bmatrix} \qquad 2.42$$

$$\mathbf{x}_i^{static} = -\mathbf{K}_{ii}^{-1}\mathbf{K}_{ib}\mathbf{x}_b = \mathbf{\Lambda}_c\mathbf{x}_b, \qquad 2.43$$

Where $\mathbf{x}_i$ and $\mathbf{x}_b$ are displacement vectors of interior and boundary DOFs, respectively, and $\mathbf{K}$ is the stiffness matrix of the fundamental sector. $-\mathbf{K}_{ii}^{-1}\mathbf{K}_{ib}$ is the static condensation matrix introduced in [36]. The constraint modes can also be calculated around a specific frequency (see [37]).

Attachment and Residual Attachment Modes:

As a counterpart of the constraint modes, the attachment modes are a static set of vectors that, along with the free-interface vibration modes, build the reduction basis for the so-called free-interface reduction methods. The calculation of the attachment modes and the free-interface vibration Modes does not include partitioning DOFs of a substructure. Consequently, free-interface reduction methods are generally of great interest for experimental analysis since their validation is much easier [38].

In order to calculate the attachment modes, boundary forces are added to the set of a substructure's DOFs.

$$\mathbf{u} = \begin{Bmatrix} \mathbf{x} \\ \mathbf{f}_b \end{Bmatrix} \qquad 2.44$$

Where $\mathbf{f}_b$ is the vector of boundary forces. The static equation of motion can be derived as follows:

$$\begin{bmatrix} \mathbf{K} & -\mathbf{A}^T \\ -\mathbf{A} & \mathbf{0} \end{bmatrix} \begin{Bmatrix} \mathbf{x} \\ \mathbf{f}_b \end{Bmatrix} = \begin{Bmatrix} \mathbf{f} \\ \mathbf{0} \end{Bmatrix} \qquad 2.45$$

In the above equation, $\mathbf{K}$ is the stiffness matrix of the component, and $\mathbf{A}$ is a Boolean matrix picking the boundary DOFs from the total DOFs of the component. By considering no external forces (other than boundary forces, i.e., $\mathbf{f} = \mathbf{0}$), the displacement field of the structure can be calculated in terms of a part of the flexibility matrix and interface forces:

$$\mathbf{u}^{static} = \mathbf{K}^{-1}\mathbf{A}^{T}\mathbf{f}_{b} = \mathbf{\Lambda}_{a}\mathbf{f}_{b} \tag{2.46}$$

It is noteworthy that the calculation of the $\mathbf{K}^{-1}$ is the main culprit of the high computational cost of the free-interface methods. Since there are no displacement constraints on the stiffness matrix, it will become semi-positive definite in some scenarios, and its determinant will become zero, making the direct inversion nearly impossible. A method to calculate the $\mathbf{K}^{-1}$ matrix when rigid body modes are present is given in [38].

Attachment modes can be refined by subtracting the information included in the corresponding vibration modes. The idea becomes apparent by expanding the flexibility matrix by the modes shapes of the system. This can be achieved by setting the ω term in the receptance matrix to zero:

$$\mathbf{H}(\omega) = (\mathbf{K} - \omega^{2}\mathbf{M})^{-1} = \sum_{\mathrm{r}=1}^{\mathrm{N}} \frac{\boldsymbol{\phi}_{\mathrm{r}}\boldsymbol{\phi}_{\mathrm{r}}^{\mathrm{T}}}{\omega_{\mathrm{r}}^{2} - \omega^{2}} \xrightarrow{\omega = 0} \mathbf{K}^{-1} = \sum_{\mathrm{r}=1}^{\mathrm{N}} \frac{\boldsymbol{\phi}_{\mathrm{r}}\boldsymbol{\phi}_{\mathrm{r}}^{\mathrm{T}}}{\omega_{\mathrm{r}}^{2}} \tag{2.47}$$

$$\mathbf{\Lambda}_{r} = \left(\mathbf{K}^{-1} - \sum_{i=1}^{n_r} \frac{\boldsymbol{\phi}_{i}\boldsymbol{\phi}_{i}^{T}}{\omega^{2}}\right)\mathbf{A}^{T} \tag{2.48}$$

n_r is the number of retained vibration modes. Despite the normal attachment modes, the residual attachment modes are orthogonal to the retained vibration modes.

Vibration Modes

In order to account for the dynamic motion of the structures, vibration modes are added to the reduction basis. The actual means of reduction takes place in including vibration modes, where a modal truncation is applied to include a much smaller set of vibration modes. This eventually reduces the size of each component.

Vibration modes are, in fact, eigenvectors of a generalized eigenvalue problem of $\mathbf{K}$ and $\mathbf{M}$ matrices:

$$(\mathbf{K} - \omega^2\mathbf{M})\boldsymbol{\phi} = \mathbf{0} \qquad 2.49$$

Fixed-interface vibration modes ($\boldsymbol{\phi}_i$) are calculated with the fixed displacement boundary DOFs of the substructure, whereas the free-interface vibration modes ($\boldsymbol{\phi}$) are derived with free displacement boundary DOFs. One crucial problem here is the computation of the rigid body modes. If the substructure, other than the boundary with the neighbor substructure, has no other ground connection, then the calculation of the free-interface vibration modes includes the computation of the rigid body modes. Rigid body modes are the eigenvectors corresponding to the zero eigenvalues in the mentioned generalized eigenvalue problem—however, calculating the eigenvalue problem when rigid body modes exist can be time-consuming. A computationally friendly method to calculate the rigid body modes can be found in [38].

2.2.2 Reduction Methods Based on CMS

Craig-Bampton Method:

In the Craig-Bampton method, the procedure begins with partitioning the displacement DOFs of the substructure to the boundary and inner DOFs. Considering the basic vibration equation of a component as

$$\begin{bmatrix} \mathbf{M}_{ii} & \mathbf{M}_{ib} \\ \mathbf{M}_{bi} & \mathbf{M}_{bb} \end{bmatrix} \begin{Bmatrix} \ddot{\mathbf{x}}_i \\ \ddot{\mathbf{x}}_b \end{Bmatrix} + \begin{bmatrix} \mathbf{K}_{ii} & \mathbf{K}_{ib} \\ \mathbf{K}_{bi} & \mathbf{K}_{bb} \end{bmatrix} \begin{Bmatrix} \mathbf{x}_i \\ \mathbf{x}_b \end{Bmatrix} = \begin{Bmatrix} \mathbf{f}_i \\ \mathbf{f}_b \end{Bmatrix} \qquad 2.50$$

Subsequently, as described in [6], the inner DOFs are approximated as follows:

$$\mathbf{x}_i \cong \boldsymbol{\phi}_i \boldsymbol{\eta}_i + \boldsymbol{\Lambda}_c \mathbf{x}_b \qquad 2.51$$

Therefore, the Craig-Bampton (CB) reduction matrix can be derived by adding the boundary displacement DOFs to the above equation.

$$\mathbf{x} = \begin{Bmatrix} \mathbf{x}_i \\ \mathbf{x}_b \end{Bmatrix} \cong \begin{bmatrix} \boldsymbol{\phi}_i & \boldsymbol{\Lambda}_c \\ \mathbf{0} & \mathbf{I} \end{bmatrix} \begin{Bmatrix} \boldsymbol{\eta}_i \\ \mathbf{x}_b \end{Bmatrix} = \mathbf{T}_{\mathrm{CB}} \mathbf{x}_{\mathrm{CB}} \qquad 2.52$$

In the above equation, $\boldsymbol{\phi}_i$ is a truncated set of fixed-interface vibration modes as described previously.

The reduced mass and stiffness matrices of the substructure can be derived by projecting the mass and stiffness matrices to the reduction basis.

$$\mathbf{K}_{\mathrm{CB}} = \mathbf{T}_{\mathrm{CB}}^{\mathrm{T}}\, \mathbf{K}\, \mathbf{T}_{\mathrm{CB}} \qquad 2.53$$

The mass matrix will be projected to the reduction basis just like the stiffness matrix.

Finally, Eq. (2.44) becomes:

$$\mathbf{M}_{CB} \begin{Bmatrix} \ddot{\boldsymbol{\eta}}_i \\ \ddot{\mathbf{x}}_b \end{Bmatrix} + \mathbf{K}_{CB} \begin{Bmatrix} \boldsymbol{\eta}_i \\ \mathbf{x}_b \end{Bmatrix} = \mathbf{T}_{CB}^{T} \begin{Bmatrix} \mathbf{f}_i \\ \mathbf{f}_b \end{Bmatrix} \qquad 2.54$$

After reducing each component, the retained displacement boundary DOFs of each component can be used to reconnect the component. The assembly procedure in the Craig-Bampton method follows a very straightforward superelement procedure typical of finite element analysis. The reason is the availability of the displacement DOFs of each component at the interface. This feature makes the use of the Craig-Bampton method user-friendly, an advantage that draws the attention of many scientists. On the other hand, it can be understood from the formulation that if one wishes to change the boundary DOFs, the whole eigenvalue problem (which is the most time-consuming part of the calculation) should be calculated again. Another downside of Craig-Bampton is the difficulties in the experimental validation of the fixed-interface vibration modes.

Rubin Method:

Rubin's method belongs to the free-interface reduction group. It will be shown that free-interface vibration modes and residual attachment modes are going to be implemented to build the reduction matrix in this method, and the displacement of the structure is represented by a combination of static and dynamic motion. The static motion stems from the deformation of the structure due to the external forces applied at the boundaries ($\mathbf{f}_b$); the dynamic motion is derived by a modal superposition of the free-interface vibration modes of the substructure.

The procedure starts with adding a set of static equations to the vibration equation of motion.

$$\begin{bmatrix} \mathbf{M} & \mathbf{0} \\ \mathbf{0} & \mathbf{0} \end{bmatrix} \begin{Bmatrix} \ddot{\mathbf{x}} \\ \ddot{\mathbf{f}}_b \end{Bmatrix} + \begin{bmatrix} \mathbf{K} & \mathbf{0} \\ \mathbf{0} & \mathbf{0} \end{bmatrix} \begin{Bmatrix} \mathbf{x} \\ \mathbf{f}_b \end{Bmatrix} = \begin{Bmatrix} \mathbf{f} \\ \mathbf{0} \end{Bmatrix} \qquad 2.55$$

Now the intact displacement field of the substructure can be approximated as

$$\mathbf{x} \cong \mathbf{\Lambda}_r \mathbf{f}_b + \sum_{i=1}^{n_r} \boldsymbol{\phi}^i \, \boldsymbol{\eta}^i \qquad 2.56$$

In the above equation, n_r is the retained number of the vibration modes. Finally, the first Rubin reduction matrix can be calculated as:

$$\begin{Bmatrix} \mathbf{x} \\ \mathbf{f}_b \end{Bmatrix} \cong \begin{bmatrix} \sum_{i=1}^{n_r} \boldsymbol{\phi}^i & \mathbf{\Lambda}_r \\ \mathbf{0} & \mathbf{I} \end{bmatrix} \begin{Bmatrix} \boldsymbol{\eta} \\ \mathbf{f}_b \end{Bmatrix} \qquad 2.57$$

At this point, one may realize that displacement boundary DOFs are not explicitly available after the modal truncation. Instead, boundary forces provide the information required at the boundaries. Although the coupling of the structure by the use of the boundary forces is applicable at this point, in the Rubin method, a second transformation is proposed to reintroduce the displacement boundary DOFs.

Considering Eq. (2.48), one can write:

$$\mathbf{x}_b = \mathbf{A}\mathbf{x} = \mathbf{A}(\mathbf{\Lambda}_r \mathbf{f}_b + \sum_{i=1}^{n_r} \boldsymbol{\phi}^i \, \boldsymbol{\eta}^i) \qquad 2.58$$

By calculating the $\mathbf{f}_b$ term and reinterring it to the Eq. (2.49), the second Rubin transformation matrix is derived:

$$\begin{Bmatrix} \boldsymbol{\eta}_r \\ \mathbf{f}_b \end{Bmatrix} = \begin{bmatrix} \mathbf{I} & \mathbf{0} \\ (\mathbf{A}\boldsymbol{\Lambda}_r)^{-1}\mathbf{A}\sum_{i=1}^{n_r} \boldsymbol{\phi}^i & (\mathbf{A}\boldsymbol{\Lambda}_r)^{-1} \end{bmatrix} \begin{Bmatrix} \boldsymbol{\eta}_r \\ \mathbf{x}_b \end{Bmatrix} \tag{2.59}$$

Finally, one can write

$$\begin{aligned} \begin{Bmatrix} \mathbf{x} \\ \mathbf{f}_b \end{Bmatrix} &\cong \begin{bmatrix} \sum_{i=1}^{n_r} \boldsymbol{\phi}^i & \boldsymbol{\Lambda}_r \\ \mathbf{0} & \mathbf{I} \end{bmatrix} \begin{bmatrix} \mathbf{I} & \mathbf{0} \\ (\mathbf{A}\boldsymbol{\Lambda}_r)^{-1}\mathbf{A}\sum_{i=1}^{n_r} \boldsymbol{\phi}^i & (\mathbf{A}\boldsymbol{\Lambda}_r)^{-1} \end{bmatrix} \begin{Bmatrix} \boldsymbol{\eta}_r \\ \mathbf{x}_b \end{Bmatrix} \\ &= \mathbf{T}_R \begin{Bmatrix} \boldsymbol{\eta}_r \\ \mathbf{x}_b \end{Bmatrix} \end{aligned} \tag{2.60}$$

After the second transformation, the coupling procedure will follow the straightforward superelement method, well known in finite element analysis.

Dual Craig-Bampton Method

As mentioned in the previous section, one may wish to couple the structures using the interface forces. This is the main idea of the Dual Craig-Bampton method [39].

The principal reduction and approximation are the same as the Rubin method, but an equation is added to the second row of Eq. (2.43). Adding the mentioned row of the equations enhances symmetry and enforces compatibility during assembly[38].

$$\begin{bmatrix} \mathbf{M} & \mathbf{0} \\ \mathbf{0} & \mathbf{0} \end{bmatrix} \begin{Bmatrix} \ddot{\mathbf{x}} \\ \ddot{\mathbf{f}}_b \end{Bmatrix} + \begin{bmatrix} \mathbf{K} & -\mathbf{A}^T \\ -\mathbf{A} & \mathbf{0} \end{bmatrix} \begin{Bmatrix} \mathbf{x} \\ \mathbf{f}_b \end{Bmatrix} = \begin{Bmatrix} \mathbf{f} \\ -\mathbf{x}_b \end{Bmatrix} \tag{2.61}$$

The assembly of the substructure through the boundary forces is achieved utilizing “dual assembly.” A detailed description of the dual assembly and its difference from the standard primal assembly is given in [40].

In the first step, the signed Boolean matrices (**B**) should be derived for each component (see [40]). Subsequently, mass and stiffness matrices of the substructures are mounted in the following manner:

$$\mathbf{M} = \begin{bmatrix} \mathbf{M}_{blade} & \mathbf{0} & \mathbf{0} \\ \mathbf{0} & \mathbf{M}_{disk} & \mathbf{0} \\ \mathbf{0} & \mathbf{0} & \mathbf{0} \end{bmatrix} \quad \mathbf{K} = \begin{bmatrix} \mathbf{K}_{blade} & \mathbf{0} & \mathbf{B}_{blade}^T \\ \mathbf{0} & \mathbf{K}_{disk} & \mathbf{B}_{disk}^T \\ \mathbf{B}_{blade} & \mathbf{B}_{disk} & \mathbf{0} \end{bmatrix} \tag{2.62}$$

Subscripts in the above equation indicate the blade and disk components. Finally, the DCB transformation matrix can be derived.

$$\begin{Bmatrix} \mathbf{x} \\ \mathbf{g}_b \end{Bmatrix} = \begin{bmatrix} \sum_{i=1}^{n_r} \boldsymbol{\phi}^i & \mathbf{0} & \left(\mathbf{K}_{blade}^{-1} - \sum_{i=1}^{n_r} \frac{\boldsymbol{\phi}_i \boldsymbol{\phi}_i^T}{\omega_r^2} \right) \mathbf{B}_{blade}^T \\ \mathbf{0} & \sum_{i=1}^{n_r} \boldsymbol{\phi}^i & \left(\mathbf{K}_{disk}^{-1} - \sum_{i=1}^{n_r} \frac{\boldsymbol{\phi}_i \boldsymbol{\phi}_i^T}{\omega_r^2} \right) \mathbf{B}_{disk}^T \\ \mathbf{0} & \mathbf{0} & \mathbf{I} \end{bmatrix} \begin{Bmatrix} \boldsymbol{\eta}_{blade} \\ \boldsymbol{\eta}_{disk} \\ \mathbf{g}_b \end{Bmatrix} = \mathbf{T}_{DCB} \begin{Bmatrix} \boldsymbol{\eta}_{blade} \\ \boldsymbol{\eta}_{disk} \\ \mathbf{g}_b \end{Bmatrix} \qquad 2.63$$

In Eq. (2.55), the $\mathbf{g}_b$ term stands for the global forces at the boundary. The final step is to project the mentioned stiffness and mass matrices in Eq. (2.43) into the DCB reduction basis.

$$\mathbf{K}_{\mathrm{DCB}} = \mathbf{T}_{\mathrm{DCB}}^{\mathrm{T}} \, \mathbf{K} \, \mathbf{T}_{\mathrm{DCB}} \qquad 2.64$$

The mass matrix is also projected to the reduction basis in the same manner as the stiffness matrix.

Mixed-Interface Method

From the term: “Mixed-interface method,” the method proposed in [38] is intended here, which is a mixture of the Craig-Bampton (as a fixed-interface) method and the Dual Craig-Bampton (as a free-interface) method. The motivation behind the introduction of a Mixed-interface method is the fact that, for whatever reason, one may wish to use free and fixed-interface methods simultaneously to reduce the size of a component. That is to implement fixed-interface static modes to represent a part of the boundary and free-interface static modes for the other part.

In this section, the criteria behind the selection of the fixed and free interface DOFs are the convenient coupling and elimination of the rigid body modes of the blade sector. Also, for comparing the forced vibration response of the structures in the shrouds section, the displacement of the shrouds DOFs are required. As a result, the interface boundary between the blade and disk is represented by the free interface method (Dual Craig-Bampton in this case), whereas the shrouds DOFs are held fixed.

To begin with, the displacement field of the substructure is partitioned into two sets: fixed boundaries ($\mathbf{x}_f$) and others ($\mathbf{x}_m$), boundary DOFs that are going to be represented by the Dual Craig-Bampton method are a subset of the ($\mathbf{x}_m$) since there is no need to partition the DOFs in the free-interface methods. Analogous to the Dual Craig-Bampton method, interface forces corresponding to the free boundaries ($\mathbf{f}_{free}$) are added to the total DOFs of the substructure:

$$\mathbf{x} = \begin{Bmatrix} \mathbf{x}_m \\ \mathbf{x}_f \\ \mathbf{f}_{free} \end{Bmatrix} \qquad 2.65$$

By adding the static equation of the motion to the dynamic set as the Dual Craig-Bampton routine, the equation of the motion can be written as:

$$\begin{bmatrix} \mathbf{M}_{mm} & \mathbf{M}_{mf} & \mathbf{0} \\ \mathbf{M}_{fm} & \mathbf{M}_{ff} & \mathbf{0} \\ \mathbf{0} & \mathbf{0} & \mathbf{0} \end{bmatrix} \begin{Bmatrix} \ddot{\mathbf{x}}_m \\ \ddot{\mathbf{x}}_f \\ \ddot{\mathbf{f}}_{free} \end{Bmatrix} + \begin{bmatrix} \mathbf{K}_{mm} & \mathbf{K}_{mf} & -\mathbf{A}^T \\ \mathbf{K}_{fm} & \mathbf{K}_{ff} & \mathbf{0} \\ -\mathbf{A} & \mathbf{0} & \mathbf{0} \end{bmatrix} \begin{Bmatrix} \mathbf{x}_m \\ \mathbf{x}_f \\ \mathbf{f}_{free} \end{Bmatrix} = \begin{Bmatrix} \mathbf{f}_m \\ \mathbf{f}_f \\ \mathbf{x}_{free} \end{Bmatrix} \qquad 2.66$$

A in the above equation is the Boolean matrix picking the free-interface boundary DOFs from the set of $\mathbf{x}_m$ DOFs. Finally, the approximation will be carried out on the $\mathbf{x}_m$ DOFs.

$$\mathbf{x}_m \cong \sum_{i=1}^{n_r} \boldsymbol{\phi}_m^i \, \boldsymbol{\eta}_m^i + \boldsymbol{\Lambda}_r \mathbf{f}_{free} + \boldsymbol{\Lambda}_c \mathbf{x}_f \qquad 2.67$$

It can be seen that a combination of the flexibility ($\boldsymbol{\Lambda}_r$) and constraint ($\boldsymbol{\Lambda}_c$) static modes are used to build the reduction basis. The calculation of the modes follows the same procedure in the previous section. According to Eq. (2.59), the Mixed-interface reduction matrix ($\mathbf{T}_{MXD}$) can be derived.

$$\begin{Bmatrix} \mathbf{x}_m \\ \mathbf{x}_f \\ \mathbf{f}_{free} \end{Bmatrix} = \begin{bmatrix} \sum_{i=1}^{n_r} \boldsymbol{\Phi}_m^i \boldsymbol{\eta}_m^i & \boldsymbol{\Lambda}_c & \boldsymbol{\Lambda}_r \\ \mathbf{0} & \mathbf{I} & \mathbf{0} \\ \mathbf{0} & \mathbf{0} & \mathbf{I} \end{bmatrix} \begin{Bmatrix} \boldsymbol{\eta}_m \\ \mathbf{x}_f \\ \mathbf{f}_{free} \end{Bmatrix} = \mathbf{T}_{MXD} \begin{Bmatrix} \boldsymbol{\eta}_m \\ \mathbf{x}_f \\ \mathbf{f}_{free} \end{Bmatrix} \qquad 2.68$$

Since the blade-to-disk interfaces on both components were reduced in the same manner (Dual Craig-Bampton), the coupling procedure is the same as the Dual Craig-Bampton method.

It should be noted that, by fixing the blade section from the shrouds, the component is no longer free-flowing, making the calculation of the reduced method much faster, as shown in the proceeding sections.

Modified Mixed-Interface Method

The introduction of the mixed-interface method paves the way to be more selective in choosing the reduction basis. One important criterion that can be considered in choosing the reduction basis is the vibration mode shape of the structure. It can be understood from the vibration behavior of the bladed disk assembly that the blade segment is more flexible than the disk segment. This phenomenon can be seen clearly in Figure 2.2 when the bulk of the energy and thus displacement is concentrated in the blade segment when the whole assembly vibrates in the first three natural frequencies. Consequently, the bladed disk system vibrates as if the disk segment vibrates with the free blade-to-disk interfaces, and the blade segment vibrates as if it is cantilevered from the blade root. Then it can be naturally desirable to reduce the disk segment as if no external force is exerted on it from the blade segment and, on the contrary, reduce the blade segment with its blade to disk interface held fixed [38]. In addition to the above-mentioned criterion, the assembly procedure and the availability of the displacements on shrouds DOFs are also of importance. A mixed reduction technique of the Rubin and Craig-Bampton method can meet all the aforementioned standards. A general combination of the Rubin and Craig-Bampton method has been introduced in the literature [41], and the formulation in this section is similar to the one mentioned.

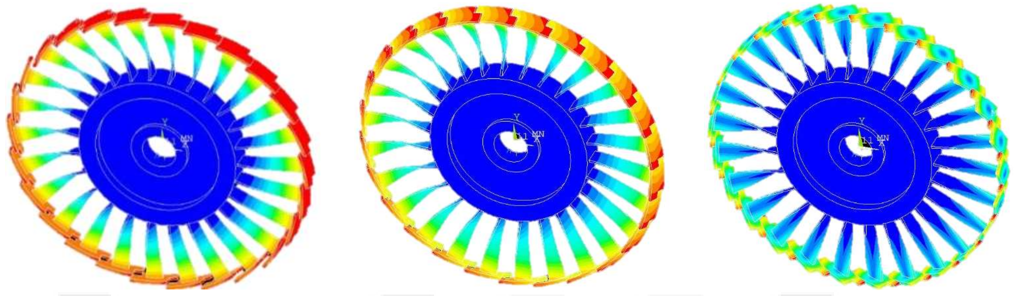

First mode Second mode Third mode

Figure 2.3. First three vibration mode for tuned bladed disk system

Similar to the Rubin method described earlier, the transformation matrix here is composed of two steps. The first transformation is the same as the Mixed-interface method of the previous section. For the second step, the forces at the free interface boundaries are going to be transformed back to the displacement in a way that is explained in the Rubin method.

$$\mathbf{x}_{free} = \mathbf{A}_{free}\mathbf{x} = \mathbf{A}_{free}\left(\sum_{i=1}^{n_r} \boldsymbol{\phi}_m^i\, \boldsymbol{\eta}_m^i + \boldsymbol{\Lambda}_r \mathbf{f}_{free} + \boldsymbol{\Lambda}_c \mathbf{x}_f\right) \tag{2.69}$$

$$\begin{Bmatrix} \mathbf{x}_m \\ \mathbf{x}_f \\ \mathbf{f}_{free} \end{Bmatrix} = \begin{bmatrix} \sum_{i=1}^{n_r} \boldsymbol{\phi}_m^i\, \boldsymbol{\eta}_m^i & \boldsymbol{\Lambda}_c & \boldsymbol{\Lambda}_r \\ \mathbf{0} & \mathbf{I} & \mathbf{0} \\ \mathbf{0} & \mathbf{0} & \mathbf{I} \end{bmatrix} \begin{Bmatrix} \boldsymbol{\eta}_m \\ \mathbf{x}_f \\ \mathbf{f}_{free} \end{Bmatrix} = \mathbf{T}_{MMXD}^1 \begin{Bmatrix} \boldsymbol{\eta}_m \\ \mathbf{x}_f \\ \mathbf{f}_{free} \end{Bmatrix} \tag{2.70}$$

According to the Eq. (2.61) the second transformation matrix can be written as:

$$\begin{Bmatrix} \boldsymbol{\eta}_m \\ \mathbf{x}_f \\ \mathbf{f}_{free} \end{Bmatrix} = \begin{bmatrix} \mathbf{I} & \mathbf{0} & \mathbf{0} \\ \mathbf{0} & \mathbf{I} & \mathbf{0} \\ (\mathbf{T}_{MMXD}^2)^{3,1} & (\mathbf{T}_{MMXD}^2)^{3,2} & (\mathbf{T}_{MMXD}^2)^{3,3} \end{bmatrix} \begin{Bmatrix} \boldsymbol{\eta}_m \\ \mathbf{x}_f \\ \mathbf{x}_{free} \end{Bmatrix} = \mathbf{T}_{MMXD}^2 \begin{Bmatrix} \boldsymbol{\eta}_m \\ \mathbf{x}_f \\ \mathbf{x}_{free} \end{Bmatrix} \qquad 2.71$$

$$(\mathbf{T}_{MMXD}^2)^{3,1} = \left(\mathbf{A}_{free}\boldsymbol{\Lambda}_r\right)^{-1} \mathbf{A}_{free} \sum_{i=1}^{n_r} (\boldsymbol{\Phi}_m^i \, \boldsymbol{\eta}_m^i) \qquad 2.72$$

$$(\mathbf{T}_{MMXD}^2)^{3,2} = -\left(\mathbf{A}_{free}\boldsymbol{\Lambda}_r\right)^{-1} \left(\mathbf{A}_{free}\boldsymbol{\Lambda}_c\right) \qquad 2.73$$

$$(\mathbf{T}_{MMXD}^2)^{3,3} = \left(\mathbf{A}_{free}\boldsymbol{\Lambda}_r\right)^{-1} \qquad 2.74$$

$$\begin{Bmatrix} \mathbf{x}_m \\ \mathbf{x}_f \\ \mathbf{f}_{free} \end{Bmatrix} = \mathbf{T}_{MMXD}^1 \mathbf{T}_{MMXD}^2 \begin{Bmatrix} \boldsymbol{\eta}_m \\ \mathbf{x}_f \\ \mathbf{x}_{free} \end{Bmatrix} \qquad 2.75$$

Since the degrees of freedom in the blade to disk interface are transformed to the displacement DOFs (like the Rubin method), the coupling procedure of the component can be carried out in its standard superelement manner.

2.2.3 Interface Reduction

The previous chapter explains how components of a structure are reduced and then assembled again to build a reduced twin of the structure. One should note that the interface DOFs are all retained in the final product of the reduction technique regardless of the type of reduction method. Occasionally, components are coupled through large interface surfaces, including numerous interface DOFs. The interface

DOFs lose their importance after the coupling process, and keeping these DOFs becomes an unwanted effort, which decreases the efficiency of the reduction method.

To address this problem, interface reduction techniques are mainly used to eliminate or at least reduce the interface DOFs.[42], [43] Thus, building more efficient reduction techniques which only carry the essential DOFs and some modal coordinates. The interface reduction techniques are usually used as a second reduction step in the reduction procedure of structures.

Principally, interface reduction can be applied both on the substructure level and after the coupling of substructures [44]. Since the interface behavior is dependent on all components that it connects, it is evident that a priori interface reduction on the component level, in general, gives far less accurate results than when information from the assembled structure is used to reduce the interface DOF. Even worse, component-level interface reduction gives rise to non-conforming interfaces, similar to non-matching element shape functions, which in turn can cause so-called interface locking if the reduction bases are poor [44]. Hence, the component level reduction is not considered in this thesis.

For the case of interface reduction after coupling components, there exist some alternatives as described below:

- The most rudimentary approach is to consider the interface to act rigidly. Thus, its motion is going to be approximated by local rigid motion. The method, also referred to as “interface rigidification,” neglects the deformation of the interface surface, making it possible to describe the interface by just six degrees of freedom [43], [44]
- As an extension to the interface rigidification, one can use some vibrational mode shapes instead of a rigid shape in cases when the deformation shape of the interface is indispensable. The method is referred to as modal reduction of the interface, and it includes an eigenvalue problem that derives the vibration modes on the interface area. Subsequently, a truncated number of vibration modes are used to describe the interface motion. It should be noted

that the vibration modes are derived after the coupling of two substructures from the interested interface area in order to have a better approximation of the interface motion. At the same time, the interface rigidification method is more suitable for conducting on the component level.

For the reasons given above and for the sake of brevity, only modal reduction of the interface is presented here. The interested reader, however, is encouraged to investigate the following articles for a more comprehensive description [45]–[47].

2.2.3.1 Modal Reduction of the Interface

The interface rigidification method may be sufficient for some unique geometries but generally is not accurate due to the oversimplification of the interface motion. In order to account for the interface deformation shape, a set of truncated static modes can be used instead of a rigid surface. The idea comes from observing that determining the interface behavior does not require in-depth insight into the component's behavior [48]. Therefore, interface modes are calculated from the coupled systems' vibration analysis while a static condensation is made on the interface DOFs [46], [49].

To begin with, consider the vibration equation of motion after coupling two reduced components.

$$\begin{bmatrix} \mathbf{M}_{ii} & \mathbf{M}_{in} \\ \mathbf{M}_{in} & \mathbf{M}_{nn} \end{bmatrix} \begin{Bmatrix} \ddot{\mathbf{x}}_i \\ \ddot{\mathbf{x}}_n \end{Bmatrix} + \begin{bmatrix} \mathbf{K}_{ii} & \mathbf{K}_{in} \\ \mathbf{K}_{in} & \mathbf{K}_{nn} \end{bmatrix} \begin{Bmatrix} \mathbf{x}_i \\ \mathbf{x}_n \end{Bmatrix} = \begin{Bmatrix} \mathbf{f}_i \\ \mathbf{f}_n \end{Bmatrix} \qquad 2.76$$

In the above equation, subscript i denotes the DOFs on the interface, and n denotes the other degrees of freedom on the two substructures. Subsequently, the equation of motion is condensed on the interface DOFs by taking the interface portion of the equation.

$$\mathbf{M}_{ii}\ddot{\mathbf{x}}_i + \mathbf{K}_{ii}\mathbf{x}_i = \mathbf{f}_i \qquad 2.77$$

It can be shown mathematically that, $\mathbf{M}_{ii}$ and $\mathbf{K}_{ii}$ are the static condensations for Rubin and Craig-Bampton methods [46]. This can be extended to the MMXD method case, sine the MMXD method is actually a generalization of Rubin and Craig-Bampton methods. Concretely, the interface modes are either static constraint modes or attachment modes. The above equation can be considered the assembled system interface while no vibration modes are included. The reason is that each component interface is actually computed using static interface modes. Therefore, the equation can be used to derive the interface's behavior by assuming zero external forcings.

$$(\mathbf{K}_{ii} - \omega^2 \mathbf{M}_{ii})\boldsymbol{\phi} = \mathbf{0} \qquad 2.78$$

Here, ω is the frequency, and $\boldsymbol{\phi}$ is the interface displacement mode. In line with all CMS reduction methods, the reduction is obtained by truncating the number of interface modes shapes.

$$\mathbf{x}_i \approx \sum_{r=1}^{n} \boldsymbol{\phi}_r \eta_r = \boldsymbol{\Phi}\boldsymbol{\eta}_i \qquad 2.79$$

The interface reduction basis will take the form:

$$\begin{Bmatrix} \mathbf{x}_i \\ \mathbf{x}_n \end{Bmatrix} = \begin{bmatrix} \boldsymbol{\Phi} & \mathbf{0} \\ \mathbf{0} & \mathbf{I} \end{bmatrix} \begin{Bmatrix} \boldsymbol{\eta}_i \\ \mathbf{x}_n \end{Bmatrix} = \mathbf{T}_{int} \begin{Bmatrix} \boldsymbol{\eta}_i \\ \mathbf{x}_n \end{Bmatrix} \qquad 2.80$$

The above formulation is the conventional interface reduction method by using modal truncation. However, one may notice that the interface reduction eliminates the coupling between the interface DOFs and the rest. In case that there is no actual coupling between these coordinates, the method gives accurate results (like the case in the Craig-Bampton method). However, if the coupling terms exist, the conventional formulation results in rigidification and increased natural frequencies [50]. Consequently, an improved formulation is given in this section based on fixed interface reduction that works well for all the reduction techniques. The proposed interface reduction method can be considered as an enhanced modal interface reduction method.

In this new formulation, the approximation for the interface behavior is derived using the approximation made in the Craig-Bampton method. By doing so, the intercoupling terms can be preserved on the final reduction product.

$$\mathbf{x}_i \approx \sum_{r=1}^{n} \boldsymbol{\phi}_r \eta_r + \boldsymbol{\Lambda}_c \mathbf{x}_n = \boldsymbol{\Phi}\boldsymbol{\eta}_i + \boldsymbol{\Lambda}_c \mathbf{x}_n \tag{2.81}$$

$$\boldsymbol{\Lambda}_c = -\mathbf{K}_{ii}^{-1}\mathbf{K}_{in} \tag{2.82}$$

By using the new approximation, the enhanced interface reduction basis can be derived as

$$\begin{Bmatrix} \mathbf{x}_i \\ \mathbf{x}_n \end{Bmatrix} = \begin{bmatrix} \boldsymbol{\Phi} & \boldsymbol{\Lambda}_c \\ \mathbf{0} & \mathbf{I} \end{bmatrix} \begin{Bmatrix} \boldsymbol{\eta}_i \\ \mathbf{x}_n \end{Bmatrix} = \mathbf{T}_{int}^{N} \begin{Bmatrix} \boldsymbol{\eta}_i \\ \mathbf{x}_n \end{Bmatrix} \tag{2.83}$$

In the above equation, N superscripts denote the new interface reduction basis to distinguish from the conventional one. During this thesis, the proposed interface reduction is used for all of the interface reduction procedures.

2.3 Mistuning Modeling

In realistic turbomachinery systems, there are minor deviations in the geometrical properties of the sectors from the nominal designed system. These differences are mainly due to inevitable tolerances in manufacturing, non-uniform operational wear, and inhomogeneous material properties [51]. The mentioned circumstances cause mistuning phenomena, which means that the sector is not ideally tuned, and there are some discrepancies between them.

Mistuning phenomena is of immense importance since it causes localization. In tuned systems where the sectors are ideally identical, the system poses multiple natural frequencies. This means that the energy will scatter among the sectors equally. The uniform distribution reduces the amount of energy concentration on a single sector, and as a result, a lower deformation is imposed on each sector. Mistuning, on the other hand, breaks the symmetry down. In the mistuned systems, there exist one or some blades that are more flexible than the others. Thus, their vibration energy level place lower than the others. Consequently, vibration energy concentrates on the mentioned sectors, and higher deformation is imposed on a small number of blades. Localization phenomena can be hazardous when mistuning is not taken into consideration in the design process.

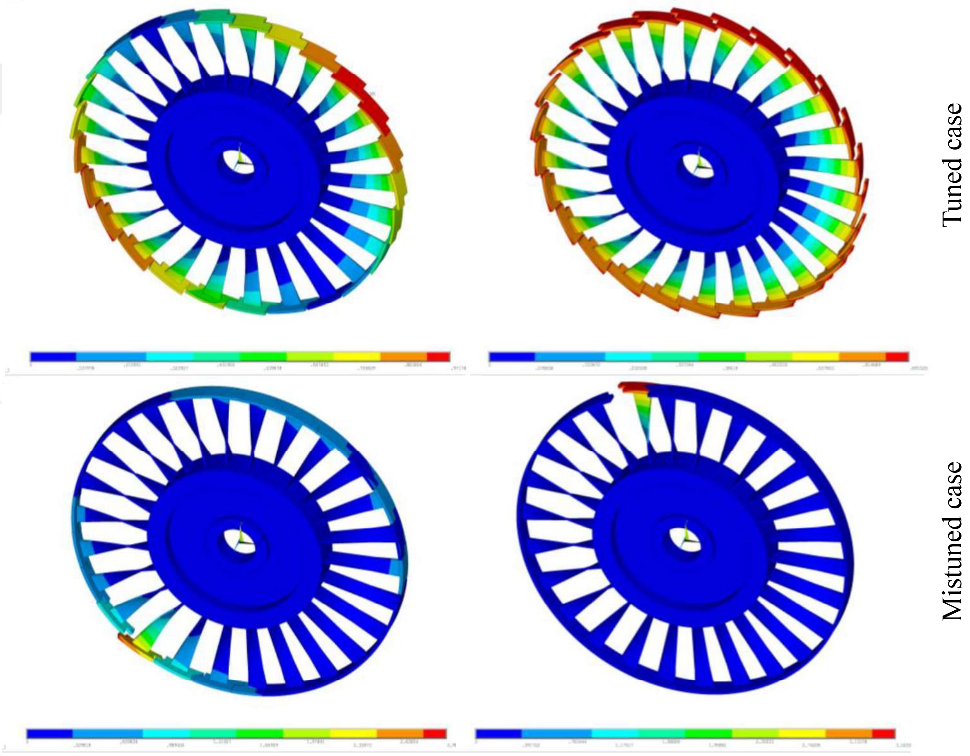

Figure 2.4. Localization phenomena in mistuned bladed disk systems

In order to build a more realistic model of the turbomachinery, mistuning should be included. There are several drawbacks of including mistuning to the equation of motion:

- Including mistuning means that cyclic symmetry is no longer valid. With cyclic symmetry, the convenience it brought in terms of computational time and required storage is also gone for the mistuned analysis.

- Mistuning by nature is a random phenomenon. Randomness makes the modeling of the mistuning much more difficult. Typically, a statistical analysis like Monte-Carlo is carried out to account for the randomness in the mistuning patterns. Such statistical investigations usually require the solution of the problem millions of times for different mistuning patterns [52], [53].

The factors mentioned above make the reduced-order modeling much more demanding for the mistuned case. Therefore, more sophisticated reduction techniques are implemented to create efficient reduced-order models for mistuned cases.

There are different methods to model mistuning [54], [55]. In fact, there are different mistuning patterns, some more severe than the others [56]. In this thesis and most of the research in the literature, mistuning is modeled as a structural modification to the tuned system [57]–[59]. Specifically, for small mistuning, this geometrical modification is done by perturbating Young's modulus (E). The multiplication of the stiffness matrix can imply perturbation on the E modulus by the ratio of change in the E modulus. Alternatively, this can be done by perturbing the natural frequency values correspondingly for modal reduction techniques.

It should also be noted that mistuning is applied on the blade sector only, since the disk sector is usually one bulky structure and is less prone to the mistuning phenomena.

Two randomly distributed mistuning patterns are considered in this study, namely $\mathbf{p}_1$, and $\mathbf{p}_2$. The former is a random mistuning pattern with a uniform distribution, and the latter is a random pattern with a normal distribution. The values of each pattern can be found in the below table.

Table 2.1 Young modulus ratio for two different mistuning patterns

Pattern #1			
Blade#	ratio	Blade#	ratio
1	1.0980	14	0.9220
2	0.8750	15	1.0030
3	1.0750	16	1.0040
4	0.8730	17	1.1270
5	0.9470	18	1.1180
6	1.0500	19	1.0580
7	1.1120	20	0.9510
8	0.8320	21	1.1250
9	1.1720	22	1.0130
10	1.110	23	0.9400
11	0.9950	24	1.1760
12	0.9740	25	1.1510
13	0.9790	26	1.0200

Pattern #2			
Blade#	ratio	Blade#	ratio
1	0.9285	14	1.0791
2	1.1351	15	0.8668
3	0.9775	16	0.7670
4	0.9411	17	0.8551
5	0.9706	18	1.0333
6	0.9152	19	1.0391
7	0.8879	20	1.0452
8	1.2526	21	0.9869
9	1.1655	22	1.0148
10	1.0307	23	0.9524
11	0.8742	24	1.0862
12	0.9134	25	0.8638
13	0.9823	26	1.0455

The ratio values given in the above table are actually the ratio of the blade's E modulus to the E modulus of the tuned system. Since the stiffness matrices for each blade are in hand after the reduction procedure, the ratio will be multiplied directly by the stiffness matrix of each blade.

$$\mathbf{K}^b = \begin{bmatrix} r_1\boldsymbol{k}^b & \mathbf{0} & \dots & \mathbf{0} \\ \mathbf{0} & r_1\boldsymbol{k}^b & \dots & \mathbf{0} \\ \vdots & \vdots & \ddots & \mathbf{0} \\ \mathbf{0} & \mathbf{0} & \mathbf{0} & r_N\boldsymbol{k}^b \end{bmatrix} \qquad 2.84$$

In the above equation, r_i denotes the E modulus ratio given in Table 2.1. The i subscript indicates the blade number.

CHAPTER 3

CASE STUDIES

In this chapter, first, a description of the finite element model is provided upon which the reduction procedure will be implemented. Subsequently, a reduction procedure is described for a bladed disk assembly where the cyclic symmetry property is held on both disk and blade segments. For the case of a tuned bladed disk system, different reduction methods are implemented to reduce the size of the system. In a later chapter, a comparative investigation of these methods is given. Finally, the last section is devoted to the mistuning case, where the cyclic symmetric property does not hold for the blade segments. The mistuning effect significantly increases the computational burden highlighting the need for a more sophisticated reduction strategy. For this case, a combination of all the methods seen in the previous chapter is capitalized on, to reduce the size of the problem efficiently. Assimilate to the tuned case, different strategies are implemented to this end, and a comparison study on the approaches is provided in the next chapter.

3.1 Finite Element Model

In order to implement the methods, a rather elaborate finite element model of a bladed disk system is created on a commercial finite element software. As depicted in Figure 3.1, the model includes 26 blades, and each is in contact with both adjacent blades (left and right) through the shroud sections. This contact area is especially of importance for energy dissipation and reduction of unwanted vibration amplitude of the blades.

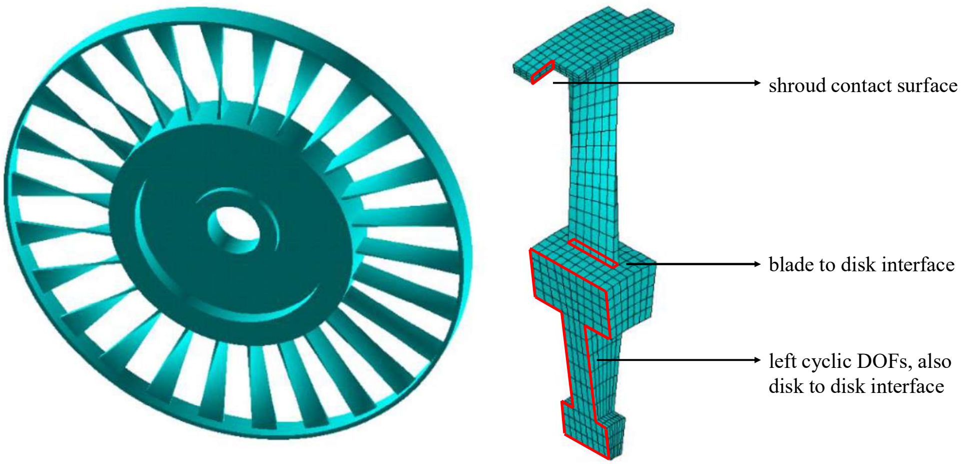

complete bladed disk assembly

fundamental sector

Figure 3.1. Nodal information and interface description for fundamental sector

The information on the model's element and material properties can be found in

Table 3.1 Nodal information of the fundamental sector

Model	**Bladed disk system with shrouds (number of blades = 26)**						
Sector	B-D interface	shrouds	D-D interface	single blade	single disk	fundamental sector	full model
Size (DOFs)	42	96	354	2,010	2,478	4,446	106,392

After creating the model in the commercial finite element software, mass and stiffness matrices of the fundamental sector are extracted. It should be noted that mass and stiffness matrices are extracted in Harwell-Boeing format. Moreover, a mapping matrix is extracted along with the matrices, which indicates the order of the degrees of freedom in the extracted mass and stiffness matrices. A computer code is developed to read all this information and provide the fundamental sector's mass and stiffness matrices.

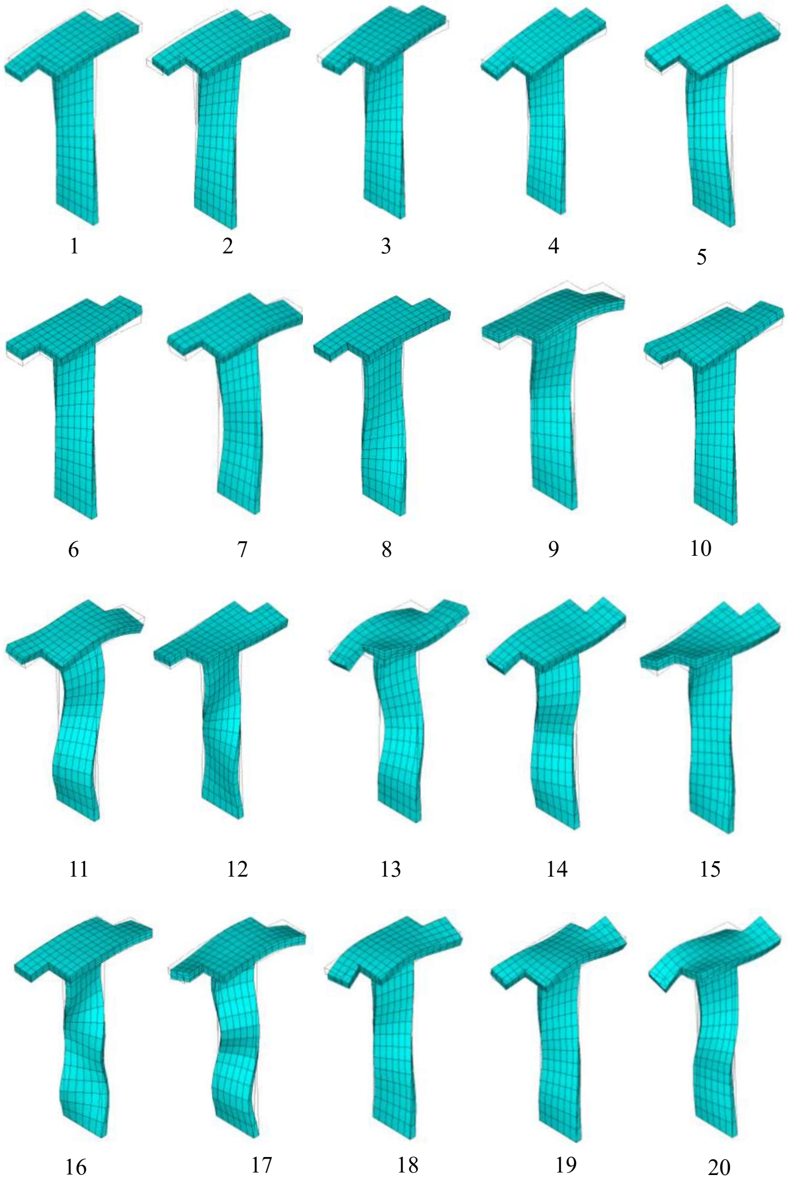

Figure 3.2. First twenty modes of the cantilever blade

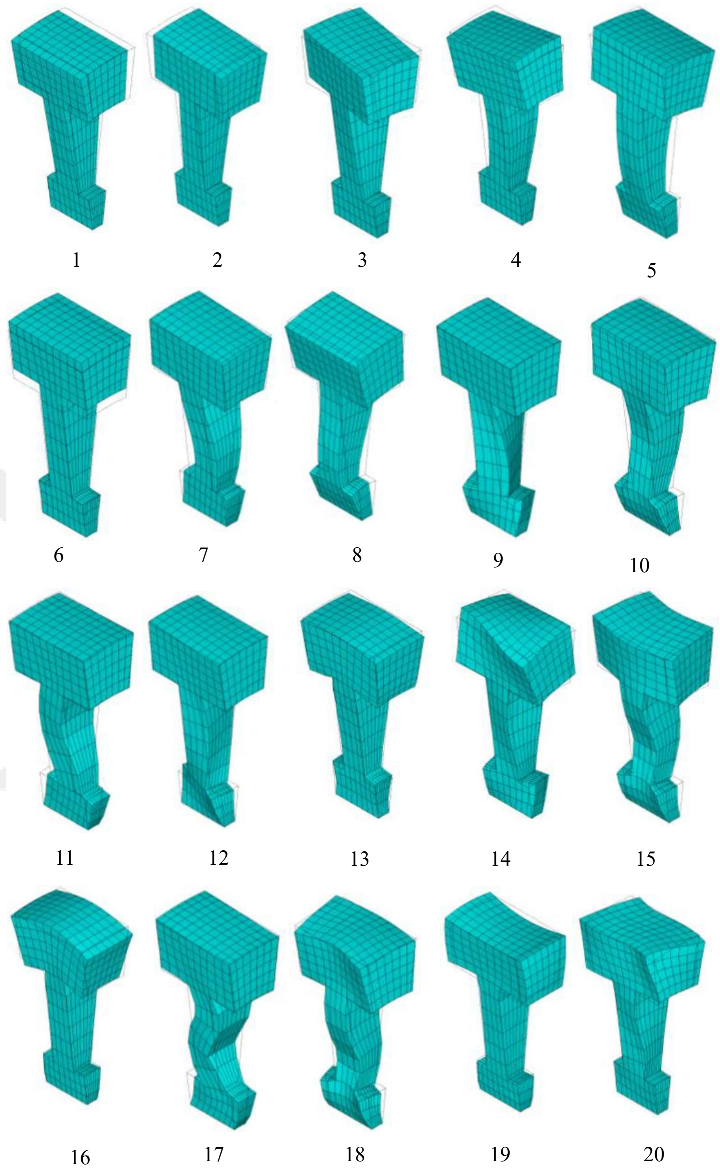

Figure 3.3. First twenty modes of the disk

3.2 Tuned Bladed Disk System

For the case of the tuned system, cyclic symmetry plays a prominent role in the reduced-order modeling of the system. The cyclic symmetric assumption not only reduces the modeling burden of the system but also provides the possibility to reduce the computational cost even further in the case of engine order excitation. As shown in the second chapter, if a cyclic symmetric structure is exposed to a type of excitation called engine order excitation, which is the typical excitation for turbomachinery systems, only one of the harmonic indices is going to have a nonzero contribution. Therefore, the size of the problem reduces to the calculation of a single harmonic index. Regardless of the excitation force, the reduction problem in this section is confined to reduced-order modeling of the fundamental sector due to the cyclic symmetry.

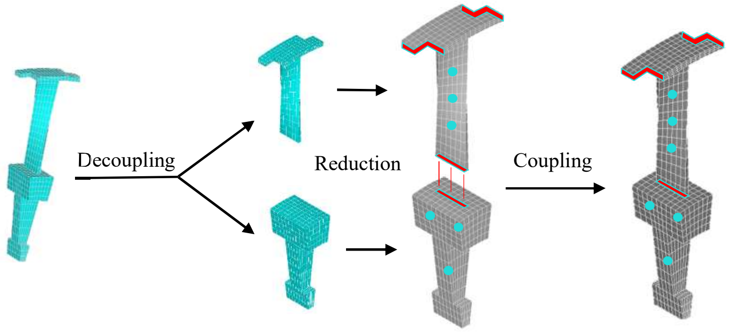

Figure 3.4. Reduction procedure based on CMS for tuned bladed disk system

To this end, all the reduction methodologies based on CMS are implemented in a procedure illustrated in Figure 3.2. That is to first reduce the entire bladed disk system (with 26 blades) to one fundamental sector for each harmonic of interest. Subsequently, reduce the size of the blade and disk component, which are represented in cyclic coordinates. Finally, the reduced components are assembled again to create the reduced fundamental sector. The procedure of coupling sectors to build the entire bladed disk system (which in this model is composed of 26 sectors) is carried out using the cyclic symmetry property (see Figure 3.2). Thus, the boundary DOFs of the neighbor sectors (disk to disk interface) are not included in the final DOFs.

Table 3.2 Reduction algorithm for tuned case

```
Algorithm TUNED SYSTEM REDUCTION
Input: mass and stiffness of fundamental blade and disk: $\mathbf{k}^d, \mathbf{m}^d$ ,  $\mathbf{k}^b, \mathbf{m}^b$
Step 1: cyclic symmetry on disk: $\mathbf{k}_h^d\,, \mathbf{m}_h^d = cyc(\mathbf{k}^d, \mathbf{m}^d),\ h = 1,2, \ldots, p$
Step 2: reduce disk and blade segments by CMS:
    $\{\mathbf{k}_{h,R}^d\,, \mathbf{m}_{h,R}^d\} = CMS(\{\mathbf{k}_h^d\,, \mathbf{m}_h^d\}), \qquad \{\mathbf{k}_R^b\,, \mathbf{m}_R^b\} = CMS(\{\mathbf{k}^b, \mathbf{m}^b\})$
Step 3: coupling and analysis on harmonic level:
    $\mathbf{K}_h^d\,, \mathbf{M}_h^d = couple(\{\mathbf{k}_{h,R}^d\,, \mathbf{m}_{h,R}^d\}, \{\mathbf{k}_R^b\,, \mathbf{m}_R^b\})$
```

3.2.1 Disk

As it has been asserted, cyclic symmetry plays an important role in the reduction procedure of the tubed bladed disk systems. Thus, the first step toward the reduced-order modeling of the disk sector is applying cyclic symmetry. In order to do so, first, the single disk sector coordinates are reordered in the manner shown below.

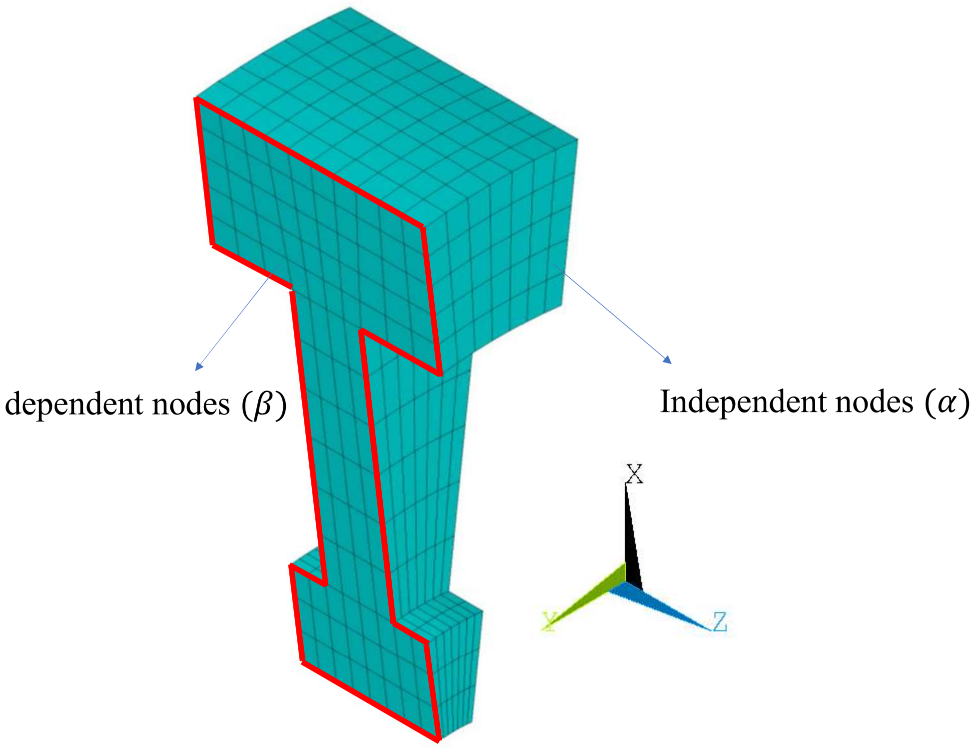

Figure 3.5. Disk segment of the fundamental sector

$$\{\mathbf{u}^d\} = \begin{Bmatrix} \mathbf{u}_\alpha^d \\ \mathbf{u}_\beta^d \\ \mathbf{u}_n^d \end{Bmatrix} \qquad 3.1$$

Then, coordinates on the dependent cyclic segment should be transformed on the independent coordinates through a rotational transformation in the cartesian frame.

$$\mathbf{u}_{\beta T}^d = \mathbf{T}_\beta \mathbf{u}_\beta^n \qquad 3.2$$

Subscript T denotes the transformed dependent coordinates. The transformation matrix takes the form:

$$\mathbf{T}_\beta = \mathbf{I}_\beta \otimes \mathbf{T} \qquad 3.3$$

In the above equation, the $\otimes$ operator corresponds to the Kronecker product, and **T** is the rotation matrix in cartesian coordinates, both of which are described in chapter two.

Finally, the total transformation of the mass and stiffness matrices will be as follows

$$\begin{Bmatrix} \mathbf{u}_{\alpha}^{d} \\ \mathbf{u}_{\beta}^{d} \\ \mathbf{u}_{n}^{d} \end{Bmatrix} = \mathbf{T}_{f} \begin{Bmatrix} \mathbf{u}_{\alpha}^{d} \\ \mathbf{u}_{\beta T}^{d} \\ \mathbf{u}_{n}^{d} \end{Bmatrix} = \mathbf{u}_{T}^{d} \tag{3.4}$$

Where the total transformation matrix will have the form

$$\mathbf{T}_{f} = \begin{bmatrix} \mathbf{I}_{\alpha} & 0 & 0 \\ 0 & \mathbf{T}_{\beta} & 0 \\ 0 & 0 & \mathbf{I}_{n} \end{bmatrix} \tag{3.5}$$

And the mass and stiffness matrices can be projected by the transformation matrix as follows

$$\mathbf{k}_{T}^{d} = (T_{f})'\mathbf{k}^{d}T_{f}, \qquad \mathbf{m}_{T}^{d} = (T_{f})'\mathbf{m}^{d}\mathbf{T}_{f} \tag{3.6}$$

The next step is to couple the disk sector through different harmonies. Following the description given in the cyclic symmetry analysis, this procedure includes coupling dependent and independent boundaries for each harmonic index. In our case, since we have 26 cyclic sections, meaning that our entire model is comprised of 26 identical sectors, we are going to have 14 different harmonies. For the sake of simple presentation, the complex form of the cyclic modeling is implemented here; however, the method is compatible with the real-valued counterpart. In contrast to the real-valued cyclic formulation where single and double harmonies exist, the formulation does not change for the single and double harmonies in the complex form. However, the matrices are going to be complex for double harmonies.

$$\mathbf{u}_{\beta T}^{d} = e^{i\phi_{h}}\mathbf{u}_{\alpha}^{d}\ , \qquad h = 1, 2, \dots, 14 \tag{3.7}$$

In the above equation, h denotes the harmonic index and ϕ_{h} is the phase angle corresponding the h^{th} harmonic.

The coupling procedure can be implemented through a proper matrix projection. In that case, the projection matrix will take the following form

$$u_T^d = \begin{Bmatrix} \mathbf{u}_\alpha^d \\ \mathbf{u}_{\beta T}^d \\ \mathbf{u}_n^d \end{Bmatrix} = \begin{bmatrix} \mathbf{I}_\alpha & 0 \\ e^{i\phi_h}\mathbf{I}_\alpha & 0 \\ 0 & \mathrm{I}_n \end{bmatrix} \begin{Bmatrix} \mathbf{u}_\alpha^d \\ \mathbf{u}_n^d \end{Bmatrix} = \mathbf{T}_{cyc}^h \mathbf{u}_{cyc}^{d,h} \qquad 3.8$$

By projecting the transformed mass and stiffness matrices by the cyclic transformation matrix, 14 sets of mass and stiffness matrices are derived for each harmonic index.

$$\mathbf{k}_h^d = \left(\mathbf{T}_{cyc}^h\right)' \mathbf{k}_T^d \mathbf{T}_{cyc}^h \qquad 3.9$$

In this step, reduction methods based on CMS are going to be implemented for each harmonic index. The procedure starts by partitioning the disk sector into the disk-blade interface and all other DOFs. Then, reduction methods based on CMS are implemented such that the blade to disk interface DOFs are considered the master DOFs.

$$\left\{\mathbf{u}_{cyc}^{d,h}\right\} = \begin{Bmatrix} \mathbf{u}_i^{d,h} \\ \mathbf{u}_n^{d,h} \end{Bmatrix} \approx \mathbf{R}_{CMS} \begin{Bmatrix} \mathbf{u}_i^{d,h} \ or \ \mathbf{g}_i^{d,h} \\ \boldsymbol{\eta}_n^{d,h} \end{Bmatrix} = \mathbf{u}_R^{d,h} \qquad 3.10$$

In the above equation, subscript R indicates the reduced coordinates, and $\mathbf{R}_{CMS}$ is the reduction basis derived by a CMS method. The resulting coordinate may differ based on the CMS method selection. In particular, $\mathbf{u}_i^{d,h}$ corresponds to displacement coordinates and $\mathbf{g}_i^{d,h}$ corresponds to forces on the blade to disk interface. A detailed description of the CMS methods and reduction basis is given in chapter two.

Finally, for the disk sector, we are going to be left with a set of mass and stiffness matrices for each harmonic index which is reduced by a specific method. Later we will see how each method performs to describe the behavior of the disk sector.

3.2.2 Blades

reduction procedure for the blade section will follow exactly the same as the disk with one significant difference. That is, the cyclic analysis yield no change in the blade sector. The reason is that there is no direct coupling between the blades, there will be no dependent and independent coordinates, and thus the cyclic transformation matrix will turn into an identity matrix. As a result, the mass and stiffness matrices for each harmonic index will equal the mass and stiffness matrices of the single sector.

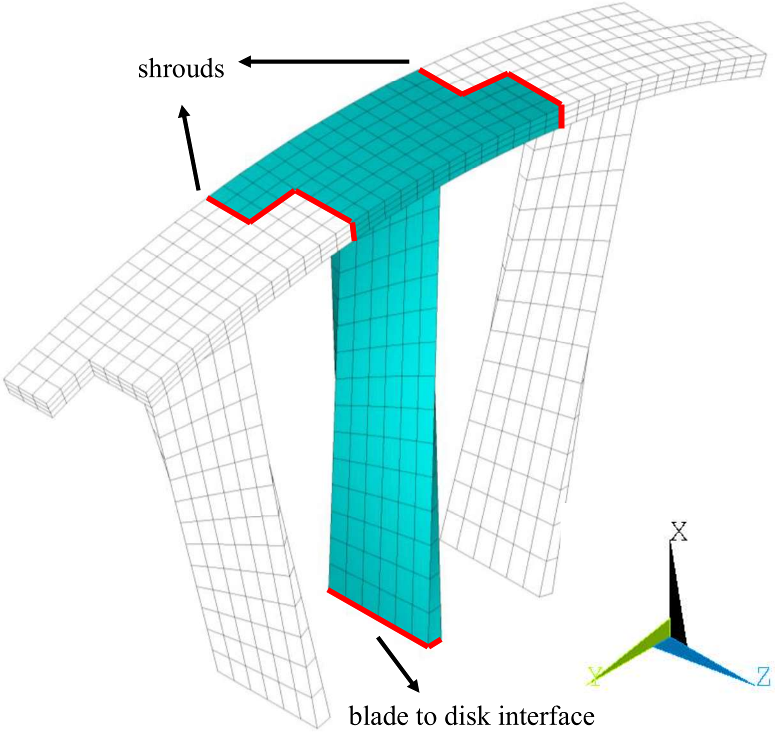

Figure 3.6. Blade segment of the fundamental sector

Analogous to the disk section, the process of reducing the blade sector starts with CMS reduction.

$$\{\mathbf{u}_{cyc}^{b,h}\} = \mathbf{u}_{cyc}^{b} = \begin{Bmatrix}\mathbf{u}_i^b\\ \mathbf{u}_n^b\end{Bmatrix} \approx \mathbf{R}_{CMS}\begin{Bmatrix}\mathbf{u}_i^b \; or \; \mathbf{g}_i^b \\ \boldsymbol{\eta}_n^b\end{Bmatrix} = \mathbf{u}_R^b \;, \qquad 3.11$$

$$h = 1, 2, \dots, p$$

Finally, after both blade and disk are reduced, they can be coupled by satisfying compatibility conditions on the blade to disk interface. The coupling will follow the description given in the second chapter.

$$\mathbf{k}_R^h = coupling\left(\mathbf{k}_R^b, \mathbf{k}_R^{d,h}\right) \qquad 3.12$$

Mass matrix will follow the exact same procedure.

3.3 Mistuned Bladed Disk System

In the dynamic analysis of turbomachinery systems, one conventional assumption is to assume that all the components of the structure are ideally identical. The cyclic symmetry property provides a considerable reduction in computational burden. As we saw in chapter 1, assuming that cyclic symmetry holds, vibration analysis of the bladed disk assembly can be confined to a single cyclic sector. This means that the matrix size is divided by the number of blades in the system. Unfortunately, previous research has shown that analysis assuming cyclic symmetry struggles to provide accurate results in practice [60]. The reason is the slight deviation in material or geometrical properties of different sectors due to manufacturing defects. These small variations are especially important in the delicate blade parts and are usually referred to as blade mistuning. The mistuning phenomena destroys the cyclic symmetric property and results in different vibrational behavior of the bladed disk systems than the one predicted by the analysis considering cyclic symmetry. In particular, the differences in the physical properties of blades lead to slightly different vibration energy levels. Therefore, the vibration of the system may confine to one or two sectors and cause much large deformation in the mentioned sectors than the one predicted by the cyclic symmetric system. The mentioned phenomenon is called localization, and it is investigated extensively in the literature[61], [62]. Consequently, it stands to reason that the mistuning effect must be included in the analysis if realistic results are demanded.

Mathematical modeling of the mistuning phenomena and their pattern is arduous due to the random nature of mistuning. As a result, scientists conduct statistical analysis like Monte Carlo, which requires solving the problem millions of times with different random mistuning patterns to derive statistical data of the system response. The acquired data is further processed to safely predict the response of the mistuned bladed disk system. The required time and storage to handle a computation of such size are huge, indicating a need for an efficient means of reduction to be implemented on the mistuned bladed disk assembly model.

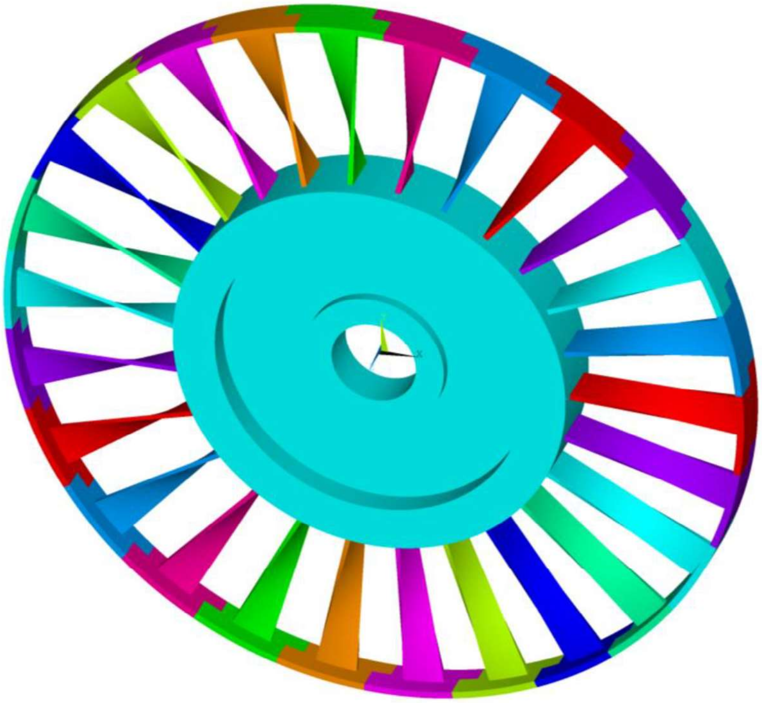

Figure 3.7. Finite element model of the mistuned bladed disk

In order to alleviate the high computational cost imposed by the circumstances mentioned above and simultaneously provide accurate results, all of the reduction methods and their combinations are considered to build an efficient reduction basis. The efficiency criteria in this study are accuracy and computational burden. Thus, all the methods are going to be compared from two distinct perspectives, computational cost and accuracy in predicting modal characteristics of the system.

Considering the specific geometry of the bladed disk systems, it is more efficient to decouple the blade and disk sector for two reasons. One, the disk sector still poses cyclic symmetry property, which can be capitalized on to reduce the computational burden of the disk segment. Two, the mistuning is implemented only on the blade, and a bladed disk assembly results in large redundant matrices. Consequently, the reduction is going to be implemented through the following procedure.

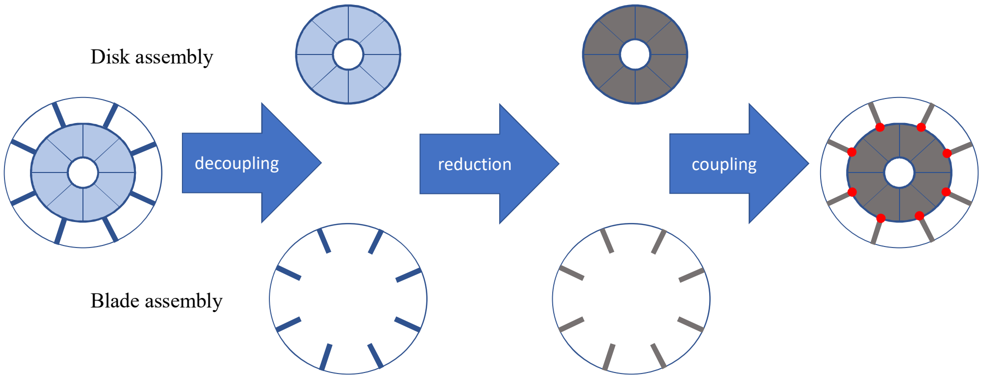

Figure 3.8. Main reduction procedure for mistuned blade disk systems

As illustrated in Figure 3.6, the entire bladed disk assembly is divided into a disk assembly that contains all disk sectors and a blade assembly that contains all the blade sectors. Subsequently, each assembly is reduced by means of CMS methods, and finally, the reduced substructures are coupled to build the reduced bladed disk model. In the proceeding section, the reduction procedure of each substructure is discussed.

3.3.1 Blades

Since there is no direct coupling between the blades, the reduction procedure will be the same as the tuned case. For the sake of brevity, here we use the results of the previous section. In the previous section, we saw that CMS methods are applied on the blade segment to provide a reduced twin model. Thus, in this section, the blades are reduced by the CMS method.

$$\mathbf{u}^b = \begin{Bmatrix} \mathbf{u}_{shr} \\ \mathbf{u}_n \\ \mathbf{u}_i \end{Bmatrix} \approx \mathbf{R}_{CMS} \begin{Bmatrix} \mathbf{u}_{shr} \\ \boldsymbol{\eta}_n \\ \mathbf{u}_i \end{Bmatrix} = \mathbf{R}_{CMS}\mathbf{u}_R^b \qquad 3.13$$

The next step is to copy each blade sector to its position in the global cartesian framework. In this step, mistuning is going to be imposed on the blade segments. After the mentioned step, the total mistuned blade substructure is going to be available in global cartesian coordinates.

$$\mathbf{U}^b = \{\mathbf{u}_{shr}^1 \quad \boldsymbol{\eta}_n^1 \quad \mathbf{u}_i^1 \quad \mathbf{u}_{shr}^2 \quad \boldsymbol{\eta}_n^2 \quad \mathbf{u}_i^2 \quad \dots \quad \mathbf{u}_{shr}^N \quad \boldsymbol{\eta}_n^N \quad \mathbf{u}_i^N\}' \qquad 3.14$$

The mass and stiffness matrices for the total blade substructure are going to be in a block diagonal form as follows:

$$\mathbf{K}^b = \begin{bmatrix} \mathbf{k}_b^1 & 0 & \dots & 0 \\ 0 & \mathbf{k}_b^2 & \dots & 0 \\ \vdots & \vdots & \ddots & 0 \\ 0 & 0 & 0 & \mathbf{k}_b^N \end{bmatrix} = blckdiag\left(k_b^i\right), \qquad i = 1,2,\dots,N \qquad 3.15$$

$$\mathbf{k}_b^i = (\mathbf{T}_i)'(\mathbf{s}_i * \mathbf{K}_b^R)\mathbf{T}_i \qquad 3.16$$

Note that in the above equation, $\mathbf{s}_i$ is the perturbation of the ith blade stemming from mistuning. $\mathbf{T}_i$ is the transformation matrix, which transforms each blade from its location in the local coordinates to global coordinates.

3.3.2 Disk

In contrast to the blade segment, cyclic symmetry still holds for the disk sector. Taking advantage of the cyclic symmetry property is vital because it provides considerable reduction without introducing any error to the equation. For the reduction of the disk sector, three different approaches are proposed, each of which is going to be elaborated on in the following.

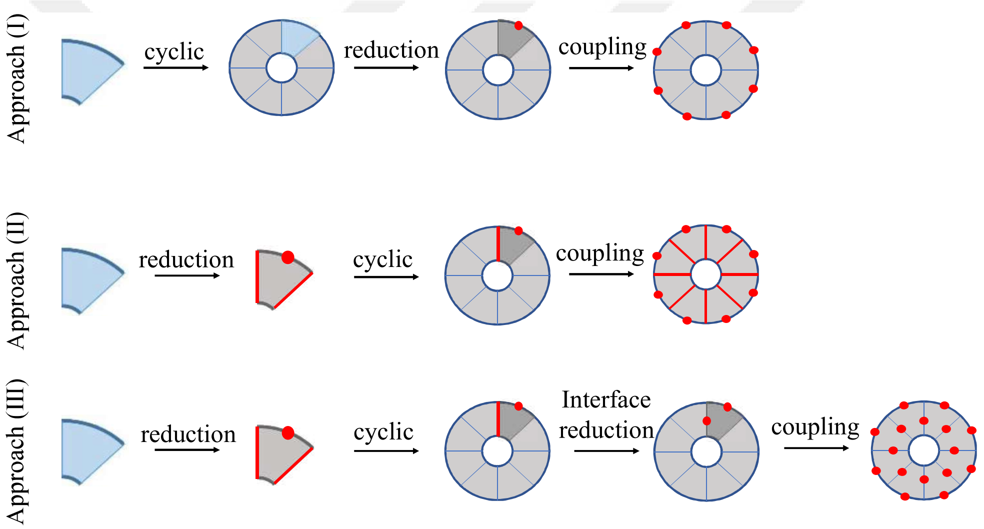

Figure 3.9. Different reduction procedures for the disk segment

APPROACH (I)

The first approach is the most straightforward and conventional one. In this method, first, the vibration equation of the disk substructure is transformed on the cyclic coordinates, as it is described in chapter one. Concretely, by applying cyclic symmetry, the vibration problem of a single large disk substructure is going to be reduced to several much small vibration problems corresponding to each harmonic index as described in the cyclic symmetry chapter. One should note that coupling of the disk sector is carried out in cyclic analysis, and the harmonic indices do not correspond to the individual disk sectors. Subsequently, for each harmonic index, reduction by CMS is implemented. For this part, both fixed and free interface methods are used as a means of reduction. Finally, the matrices of the disk sector for each harmonic index are assembled and transformed back to physical coordinates.

Table 3.3 APPROACH (I) algorithm to reduce the disk sector

```
Algorithm APPROACH (I)

Input: mass and stiffness matrices of a single disk sector
Step 1: cyclic symmetry: $\{\mathbf{k}^{d,h}, \mathbf{m}^{d,h}\} = cyc(\mathbf{k}^{d}, \mathbf{m}^{d}),\ h = 1,2,\ldots,p$
Steo 2: CMS reduction: $\{\mathbf{k}_R^{d,h}, \mathbf{m}_R^{d,h}\} = CMS(\{\mathbf{k}^{d,h}, \mathbf{m}^{d,h}\})$
Step 3: coupling and transforming back to physical coordinates: $\mathbf{K}^{d}, \mathbf{M}^{d} = couple(\{\mathbf{k}_R^{d,h}, \mathbf{m}_R^{d,h}\})$
```

One drawback of the first method is that it becomes computationally expensive in the mistuning case. The critical point here is that, in contrast to tuned vibration, where only one harmonic index contributes to the structure's forced response when exposed to engine order excitation, for the mistuned case, all of the harmonic indices do contribute to the forced vibration of the system. Thus, one needs to reduce all harmonic indices and include all, to be able to derive realistic solutions. Since the size of the disk sector is relatively large, and reduction should be applied on all the harmonic indices, one may consider reducing the disk sector prior to the cyclic symmetry implementation. The mentioned notion is the main idea of the second and third approaches.

APPROACH (II)

For the second approach, first, the sector is reduced by CMS methods to be left with disk-to-disk interface DOFs, disk-to-blade interface DOFs, and modal DOFs. For the second and third approaches, fixed, free, and nixed-interface methods are used as a means of reduction. Afterward, cyclic symmetry is carried out on the reduced disk sector, and finally, all harmonic indices of cyclic analysis are coupled and transformed back to physical coordinates.

Table 3.4 APPROACH (II) algorithm to reduce the disk sector

```
**Algorithm** APPROACH (II)
**Input:** mass and stiffness matrices of a single disk sector
Step 1: CMS reduction: $\left(\mathbf{k}_R^d, \mathbf{m}_R^d\right) = CMS(\mathbf{k}^d, \mathbf{m}^d)$
Step 2: cyclic symmetry: $\left\{\mathbf{k}_R^{d,h}, \mathbf{m}_R^{d,h}\right\} = cyc\left(\mathbf{k}_R^d, \mathbf{m}_R^d\right),\ h = 1,2,\ldots,p$
Step 3: coupling and transforming back to physical coordinates: $\mathbf{K}^d, \mathbf{M}^d = couple(\{\mathbf{k}_R^{d,h}, \mathbf{m}_R^{d,h}\})$
```

The drawback of the second approach is that, since CMS reduction is applied before cyclic analysis, the dispensable disk-to-disk DOFs are left on the final system. The unwanted interface DOFs hamper the approach's final step, which is coupling all the harmonic indices. Consequently, in the third approach, the enhanced interface reduction method introduced in chapter two is going to be implemented to reduce the disk-to-disk interface.

APPROACH (III)

Approach three follows the same steps as approach two until assembling all harmonies and transforming back to physical coordinates. Before the last step of approach two, the disk-to-disk interface is reduced by using the enhanced interface reduction technique in approach three.

Table 3.5 APPROACH (III) algorithm to reduce the disk sector

```
**Algorithm** APPROACH (III)
**Input:** mass and stiffness matrices of a single disk sector
Step 1: CMS reduction: $\left(\mathbf{k}_R^d, \mathbf{m}_R^d\right) = CMS(\mathbf{k}^d, \mathbf{m}^d)$
Step 2: cyclic symmetry: $\left\{\mathbf{k}_R^{d,h}, \mathbf{m}_R^{d,h}\right\} = cyc\left(\mathbf{k}_R^d, \mathbf{m}_R^d\right),\ h = 1,2,\ldots,p$
Step 3: perform interface reduction: $\left\{\mathbf{k}_{R,i}^{d,h}, \mathbf{m}_{R,i}^{d,h}\right\} = IR(\{\mathbf{k}_R^{d,h}, \mathbf{m}_R^{d,h}\})$
Step 4: coupling and transforming back to physical coordinates: $\mathbf{K}^d, \mathbf{M}^d = couple(\{\mathbf{k}_{R,i}^{d,h}, \mathbf{m}_{R,i}^{d,h}\})$
```

By introducing the interface reduction, the disadvantage of approach two is solved. The third approach is sought to be very efficient in terms of reduction. The performances of each approach are going to be tested in the next chapter. It should be noted that all the methods are compatible with all of the CMS reduction techniques.

CHAPTER 4

RESULTS AND DISCUSSION

In the previous chapter, the fundamental mathematics required for the reduction procedure of the structure are provided. Moreover, we have seen the different strategies to implement different reduction techniques on the specific geometry of the bladed disk system.

In this chapter, a comparison is given for all the methods and approaches mentioned in the previous chapter. First, the cyclic symmetric formulation is put on a test. The results generated by the given formulation are compared with those derived from a commercial finite element software. The following section is dedicated to the results for the tuned bladed disk system. The focal point of this section is to make an assessment of the efficiency of different reduction methods. Finally, performances of different approaches, given in the previous chapter, are compared for the case of the mistuned bladed disk system. The reduction procedure is much more demanding for the mistuned bladed disk system, requiring a set of reductions in several stages and interface reduction.

Table 4.1 Interface description by the CMS methods

Method	**Blade**		**disk**	
	B-D interface	**Shrouds**	**B-D interface**	**D-D interface**
CB	Fixed	Fixed	Fixed	Fixed
DCB	Free	Free	---	---
Rubin	Free	Free	Free	Free
Mixed	Free	Fixed	---	---
Modified Mixed	Fixed	Free	Free	Fixed

The reduction procedures mentioned in the previous chapter will be applied to the system substructure as follows.

The interface surfaces mentioned in Table 4.1 are demonstrated in the figure below

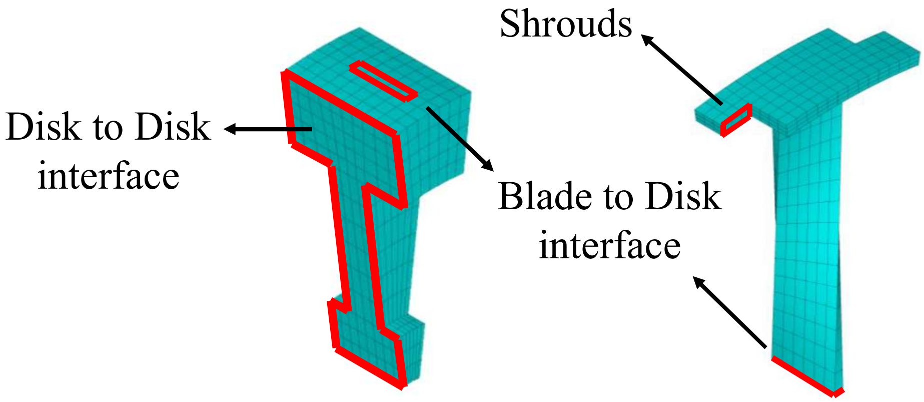

Figure 4.1. Disk to disk, shrouds, and blade to disk interface of the bladed disk assembly

In order to investigate the performance of the reduction techniques, the mass and stiffness matrices derived from each method are used for modal analysis. Natural frequencies, mode shapes, and acceptance are derived for each reduction approach in the manner described in the following.

Eigenvalue problem for the systems can be given as

$$[\mathbf{K} - \omega^2 \mathbf{M}]\phi = 0 \qquad 4.1$$

In the above equation, ω is the natural frequency, and ϕ is the mode shape vector. The receptance matrix is derived by the modal superposition

$$\sum_{r=1}^{n} \frac{\phi_r \phi_r'}{\Omega^2 - (1 + \gamma i)\omega_r^2} \qquad 4.2$$

In the above equation, Ω is the frequency at which acceptance is calculated, γ is the structural damping coefficient. The structural damping coefficient (γ) is sought to be 0.01 throughout this thesis.

For the comparison of the mode shapes, MAC numbers are calculated as shown below.

$$\mathrm{MAC}(\phi^m, \phi^n) = \frac{|\{\phi^m\}'\{\phi^n\}|^2}{(\{\phi^m\}'\{\phi^n\})(\{\phi^n\}'\{\phi^m\})} \qquad 4.3$$

4.1 Cyclic Symmetry Validation

In order to validate cyclic symmetry formulation, the cyclic analysis is carried out both on finite element software by using cyclic modeling and on MATLAB via the code generated following the given formulation. Figure 4.2 illustrates the natural frequency provided by two methods. The first ten natural frequencies for each harmonic index are derived to evaluate the cyclic symmetry formulation. The corresponding natural frequencies in each harmonic index are connected to each other to form the family modes.

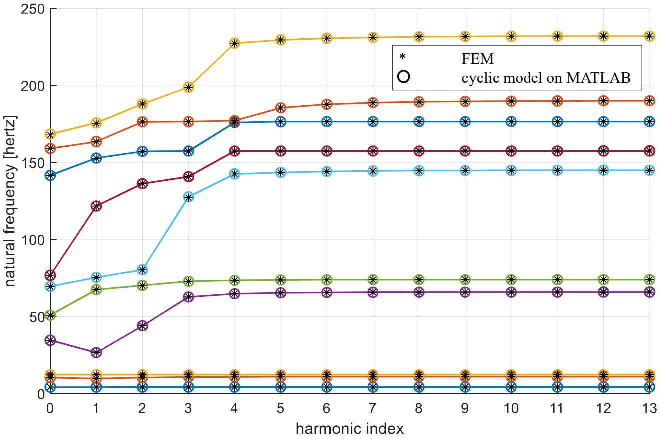

Figure 4.2. Comparison of the natural frequencies obtained from cyclic formulation and finite element model

It should be noted that cyclic symmetry does not introduce any approximation to the problem. As a result, natural frequencies obtained from the cyclic symmetry analysis exactly match the ones from FEM results.

4.2 Tuned Bladed Disk System

In this section, all the methods mentioned previously are implemented to reduce the size of an academic tuned bladed disk system.

In the first step, a perception of the computational burden of each method is provided. As shown in Table 4.2, the computational burden of the RUBIN and DCB methods is significantly higher than other methods. One very important issue in the calculation of the reduction basis is the matrix inversion for deriving the static modes. As mentioned in the Attachment Modes section, in the case of a free-floating substructure, the computation of $\mathbf{K}^{-1}$ would be computationally expensive. It should be noted that the disk component is fixed from the rotor connection DOFs, so even if the blade-to-disk connection DOFs are free (the case with Rubin, DCB, MXD, and MMXD methods), the substructure is not free-floating. However, the blade segment is supported only from the blade-to-disk interface. Thus, in the case of the Rubin and the DCB methods specifically, the inversion of the blade stiffness matrix is cumbersome. Consequently, the computation time for the Rubin and DCB methods is significantly higher than the others. Also, it should be noted that the calculation of the rigid body modes is required if a component is free-floating. Either directly from the eigenvalue problem or separately, the rigid body modes should also be calculated, which again increases the calculation burden for Rubin and DCB methods. In this study, the calculation of the rigid body modes is carried out by the eigensolver (which in this study is the ARPACK that is used by MATLAB software).

Table 4.2 Error criteria and computational time for different reduction techniques for tuned bladed disk system

Method	**Modes**	**Error% (1^{st}freq)**	**Error% (6^{th}freq)**	**Error% (9^{th}freq)**	**Comp. Time**
CB	B:12/D:1	3.14e-4	1.42e-1	5.22e-1	6.67s
	B:12/D:3	2.28e-4	6.82e-2	4.53e-1	
DCB	B:12/D:1	1.14e-3	4.86	10.6	45.35s
	B:12/D:3	1.23e-3	1.6e-3	1.40e-2	
RUBIN	B:12/D:1	1.22e-3	7.91e-2	8.49e-2	47.56s
	B:12/D:3	1.21e-3	4.54e-4	2.31e-3	
MXD	B:12/D:1	3.61e-4	4.87	**10.8**	6.57s
	B:12/D:3	3.50e-4	7.04e-2	7.01e-1	
MMXD	B:12/D:1	1.22e-3	8.10e-2	8.34e-2	6.78s
	B:12/D:3	1.21e-3	2.32e-3	**8.28e-4**	

For the second step, the modal information provided by each reduction method is going to be compared. The objective is to compare the accuracy of the methods in predicting the natural frequency and mode shapes of the system and the effect of using different dynamic and static modes on the reduction basis. Figure 4.3 depicts the accuracy of different methods in calculating the natural frequency of the system. The effect of adding more vibration modes to the reduction basis can be observed. It can be seen that the first and third natural frequencies are not affected by the disk segment. However, as we move to the higher frequencies, adding more vibration modes to the disk sector results in more accurate solutions.

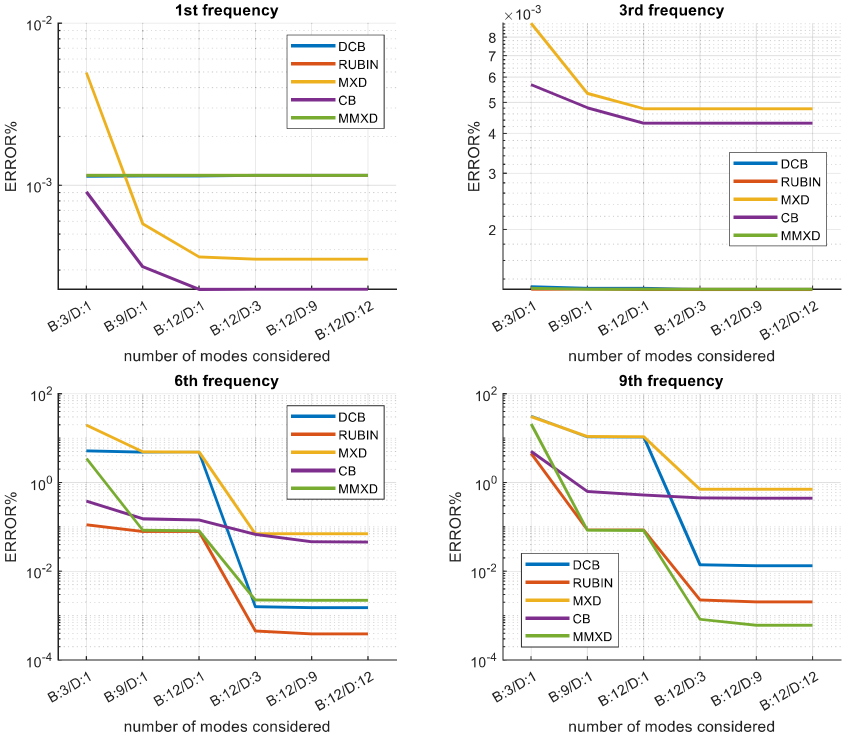

Figure 4.3. Accuracy comparison of different reduction techniques based on error criteria in predicting natural frequencies

One important phenomenon observed in this study is that the methods which describe the disk segment with fixed blade-to-disk boundary cannot improve their accuracy by adding more vibration modes to the reduction basis of the disk segment. This was, to some extent, expected since the vibration pattern of the disk segment in the entire system is closer to the vibration of the uncoupled disk segment, where it is free from the disk to blade interface. The latter can be observed by comparing the mode shapes of the disk component on both coupled and uncoupled systems. The same practice also gives invaluable information on the vibration pattern of the blade component.

As it is illustrated in Figure 4.4, in the first nine vibration modes, the disk sector is vibrating in a manner close to the first 3 to 4 vibration modes of the uncoupled disk with a free blade-to-disk interface. On the other hand, the vibration pattern of the coupled blade is better correlating with the vibration of the uncoupled blade, where the blade-to-disk interface is fixed. This information further cast light on the difference between the accuracy provided by the different methods.

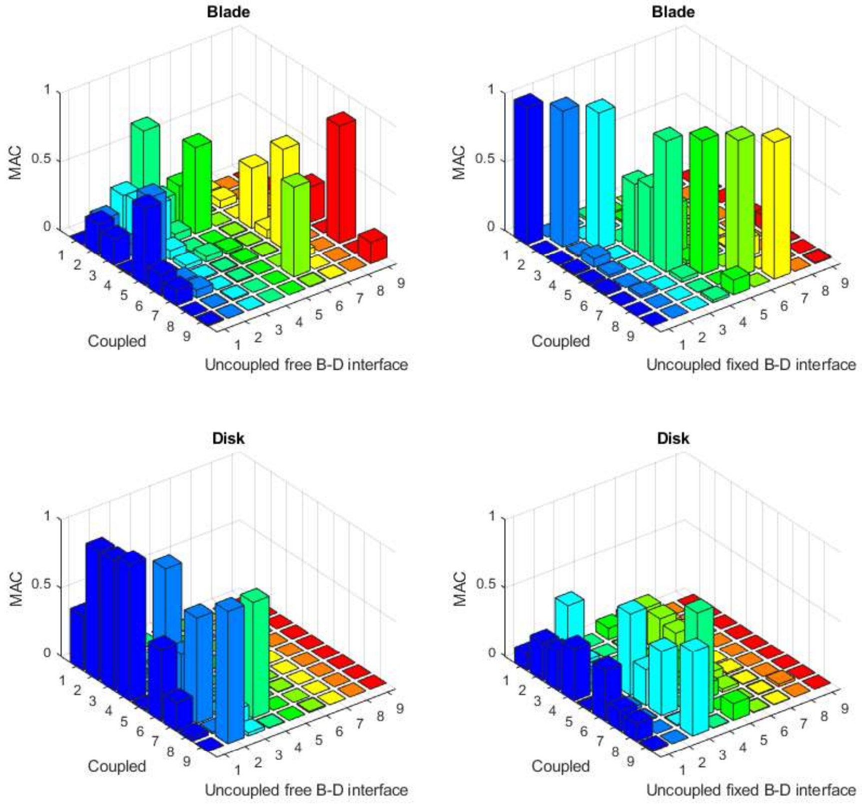

Figure 4.4. SUMAC comparison of the coupled bladed disk systems and blade nad disk sectors with fixed and free interfaces

With a similar approach, the deformation shape of the shroud segment predicted by each method is compared. The mode shapes predicted by each method are compared in Figure 4.5. The MAC numbers are calculated on the shroud DOFs only. As a result, the DCB method is not included in this comparison since shroud displacements are not included in its final DOFs (see the DCB section). From the Figure, it can be seen that the Rubin method outperforms all others. The MMXD method introduced in this paper performs better among the other three methods.

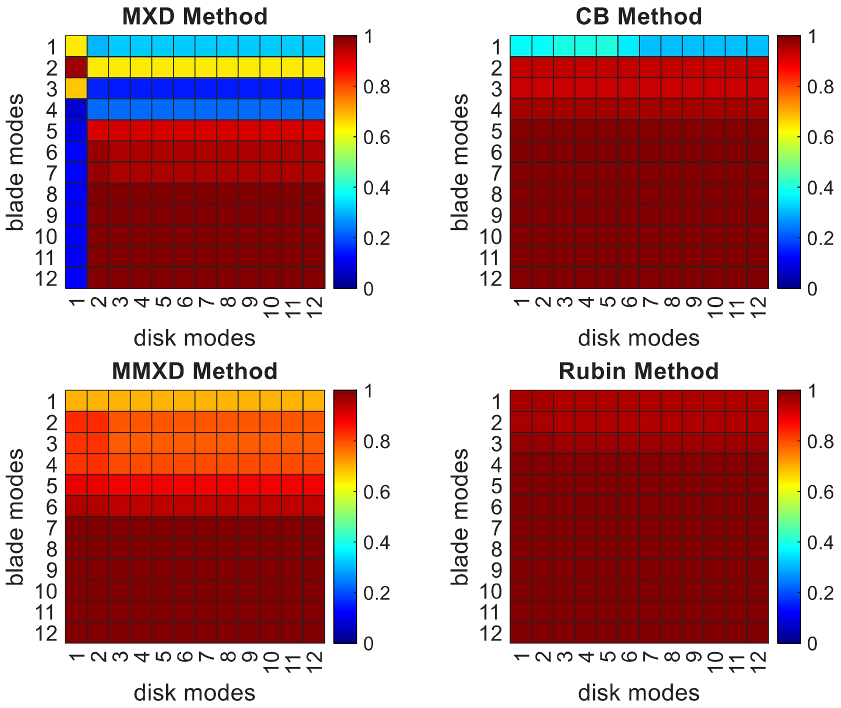

Figure 4.5. Mode shape comparison of the different reduction techniques in terms of MAC number

Finally, harmonic analysis is conducted to examine the accuracy of the reduction methods in predicting the Frequency Response Function (FRF). To this end, a unit harmonic force is applied to one of the shroud's DOFs. The response of the same DOFs to the external forcing is illustrated in Fig (6). It is evident from the figures that the MMXD method performs better than others in terms of FRF.

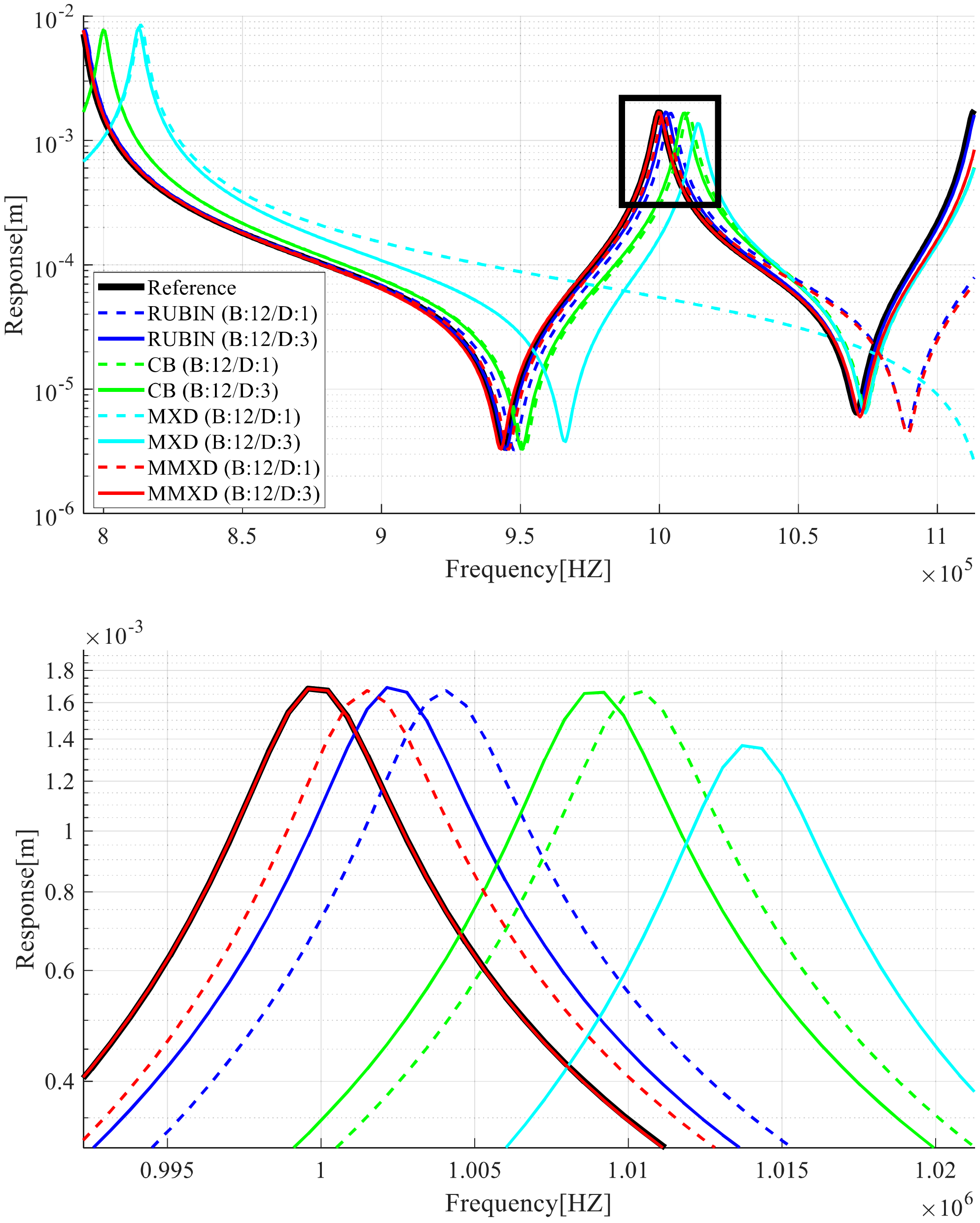

Figure 4.6. Frequency Response Function for a DOF on the shroud surface

4.3 Mistuned Bladed Disk System

For the mistuned case, as mentioned in the previous chapter, for the blade segment, only the MMXD method is used for reduction. However, since the performance of the MMXD method is not observed on the disk segment, all of the fixed, free, and mixed interface methods are used for the disk's reduction process. Specifically, this comparison study includes the Craig-Bampton, Rubin, and MMXD methods. The procedure that each reduction approach follows is depicted in the tables below step by step.

Table 4.3 Computational time and the size of matrices for each step of APPROACH (I) reduction

APPROACH (I)	Time (s)	Size (DOFs)
Step 1: cyclic	≈ 70.25s	14*2478
Step 2: CMS	≈ Rubin: 2,512s ≈ CB: 2,268s	14*62
Step 3: coupling	≈ 1.52s	1612

Table 4.4 Computational time and the size of matrices for each step of APPROACH (II) reduction

APPROACH (II)	Time (s)	Size (DOFs)
Step 1: CMS	Rubin: 8.76s CB: 5.46s MMXD: 4.68s	770
Step 2: cyclic	≈ 1.60s	14*416
Step 3: Coupling	345.74s	10,816

Table 4.5 Computational time and the size of matrices for each step of APPROACH (III) reduction

APPROACH (III)	**Time (s)**	**Size (DOFs)**
Step 1: CMS	Rubin: 8.76s CB: 5.46s MMXD: 4.68s	770
Step 2:cyclic	≈ 1.60s	14*416
Step 3: IR	10.13s	14*72
Step 4: coupling	≈ 1.84s	1,872

For the first step, analogous to the tuned case, an implication of the total computational cost and the size of the final matrices of the different methods is provided. The final results are compared in Tabel 4.6.

Table 4.6 Total computational cost and final size provided by the disk reduction methods

Methods	**Total computational time (s)**	**Final size (DOFs)**
APPROACH (I)	> 2,300s	1,612
APPROACH (II)	≈ R: 356.10 ≈ CB:352.80 ≈ MMXD: 352.02	10,812
APPROACH (III)	≈ R: 22.33s ≈ CB: 19.03s ≈ MMXD: 18.25s	1,872

The above tables provide the computational cost required for each step. Moreover, the size and number of the matrices left after each step is given. For instance, in

APPROACH (I), a cyclic analysis is first conducted, creating 14 matrices for each harmonic index. The total time for this process is around 70 seconds, and the final products are 14 sets of mass and stiffness matrices of size 2478 each. Subsequently, reduction based on CMS methods is used to reduce the size of every set of mass and stiffness matrices belonging to each harmonic index. Since the size of each set is relatively large (large for a single sector since no reduction has been made on it), the required time for this process is around 2,500 seconds. One crucial point here is that since the disk sector is not free-floating by nature (unlike the blade), the disadvantage of the free interface methods is alleviated. Concretely, free interface methods are not hampered by the rigid body modes and positive semi definiteness for the disk case. However, they still require more time than the fixed or mixed interface methods because they solve a larger eigenvalue problem (see chapter two).

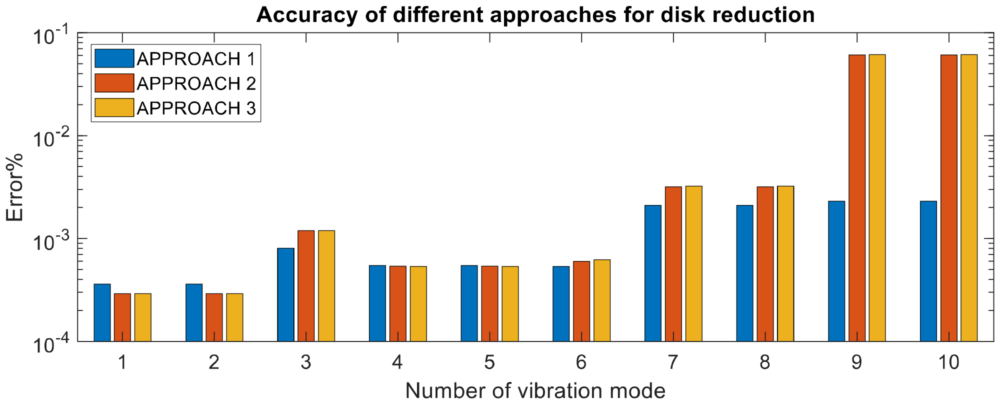

Figure 4.7. Accuracy comparison of the different reduction approaches for disk

As it is evident in Figure 4.7. the interface reduction in the third approach does not introduce much error to the reductiobn basis and thus is very efficient.

In Table 4.6, the total computational time and the final number of degrees of freedom are provided for each approach. These are critical information since an important part of the assessment is going to be determined based on this information. First, the computational cost of the first approach is incredibly high; however, this costly procedure is provided the best reduction, which means that this approach can be considered a reliable reference to calculate once and save the results. However, if a modification is applied to the system recalculating the results using this method will become arduous. Next, the second method clearly can not compete with its rivals. It is apparent that this approach needs a more effective means of reduction. Finally, the third approach provides less computational time and acceptable final results. Matrix size is not as small as the first method but pretty close. Computational-wise, however, the third approach is by far more efficient.

It should be noted that the desired output of the third approach comes with a price, and it is accuracy. More error is added to the equation since more reduction procedures are applied to the matrices. In the following subsections, the third approach's accuracy will be investigated. The reference for this investigation is the results from the first approach since only one step of the CMS reduction is applied in approach one, and this procedure has already been validated in the tuned bladed disk system section.

Modal analysis is conducted to study the accuracy provided by the third approach. Mainly, the approach will be tested for the prediction of natural frequency, mode shapes, and receptance value.

4.3.1 Zero Mistuning

For the first step, no mistuning is applied to the matrices. In order to determine if the reduction procedure is valid for general cases without using mistuning.

First, the natural frequencies provided by the reduction method are compared with the reference results. As mentioned, the reference results are derived from the first approach. As shown in Figure 4.7, overall, the Rubin method provides slightly better results than MMXD and CB methods. Nevertheless, all three methods provide excellent accuracy such that the error criteria barely surpass the 1% error line in the first 800 natural frequencies.

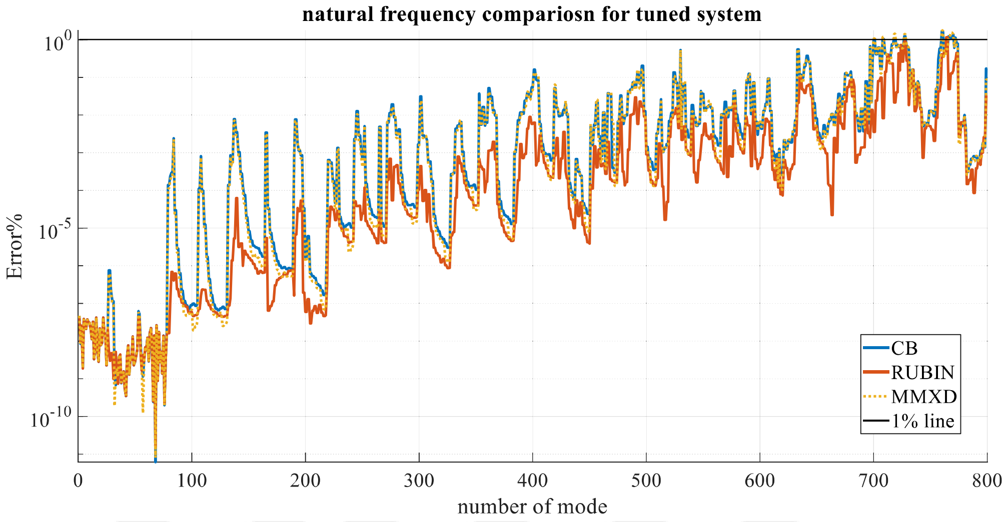

Figure 4.8. Natural frequency comparison for the case with zero mistuning

Subsequently, mode shapes on the shrouded area are compared; these mode shapes are of special importance since they are required in the nonlinear analysis stemming from friction contact between shroud contact surfaces.

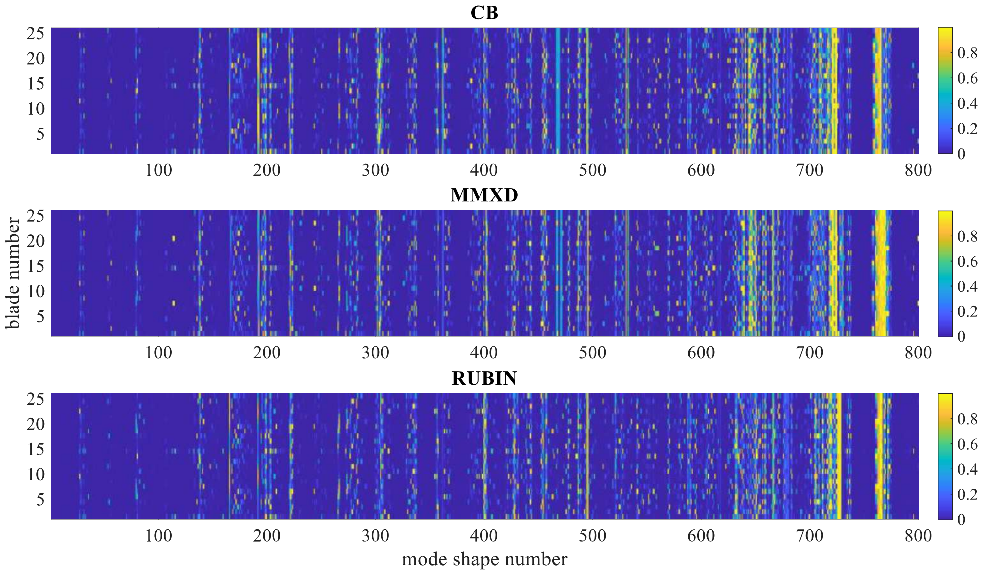

Figure 4.9. Mode shape comparison for the case with zero mistuning

Below one can find the fist number of MAC number with the specified criteria.

Table 4.7 MAC number for the case with zero mistuning

Method	0.99	0.95	0.9	0.75	0.5
CB	79	137	137	191	191
MMXD	79	137	137	192	495
RUBIN	80	138	165	165	494

The results of the mode shape comparison are depicted in Figure 4.8. In contrast to the typical structure, here, we observed a non-trivial pattern of the MAC numbers. Low MAC numbers tend to appear from lower mode shape numbers (but less frequently) to higher mode numbers. Whereas one expects to see a roughly uniform increase in the number of low MAC numbers, like in Figure 4.12. This happens as a result of the symmetry. It is of value to recall that the mode shapes considered in the reduction basis are derived from the vibration of a single sector, and truncation is made on them. Specifically for the disk sector where cyclic symmetry applies, modes shapes are derived for each harmonic index. When a mode shape of a complete system pertains to a harmonic index of higher modes than the one considered in the reduction, a low MAC number is derived.

Finally, for the case with zero mistuning, receptance values are derived to visualize the reduced-order model's ability to derive the forced response function of the system. For this step, receptance is chosen over the conventional FRF plot to show that the reduction method is not dependent on the external forcing. That is to say that, no matter if the excitation is of the engine order type or any other form of harmonic excitation, the reduction method is capable of obtaining accurate results. Furthermore, since the mass and stiffness matrices are available after this reduction, any type of structural analysis can be applied to the reduced-order model. This can be considered an advantage for CMS methods over conventional modal reduction and superposition. One node is taken arbitrarily to drive the direct receptance coefficient for, as shown in Figure 4.9.

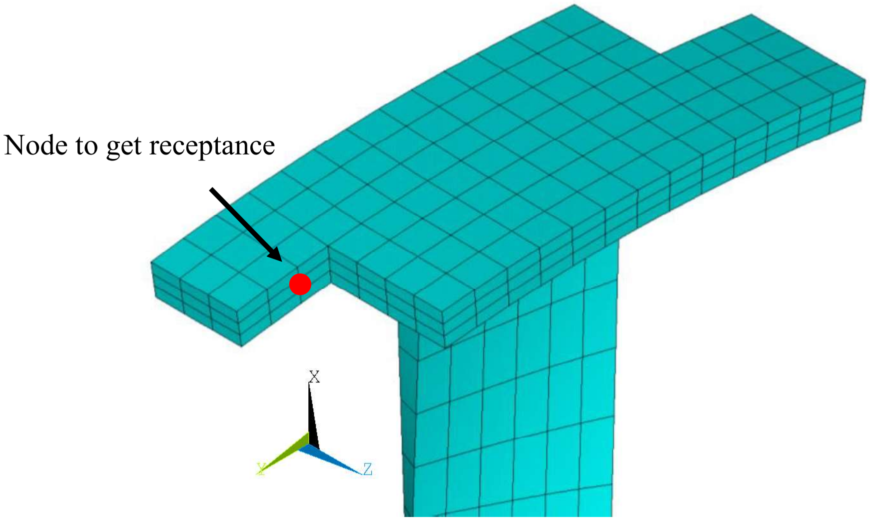

Figure 4.10. Node for which the receptance coefficient is calculated

The receptance results are shown in the below figure. As it can be seen, there is not a visible difference in the receptance results provided by the methods.

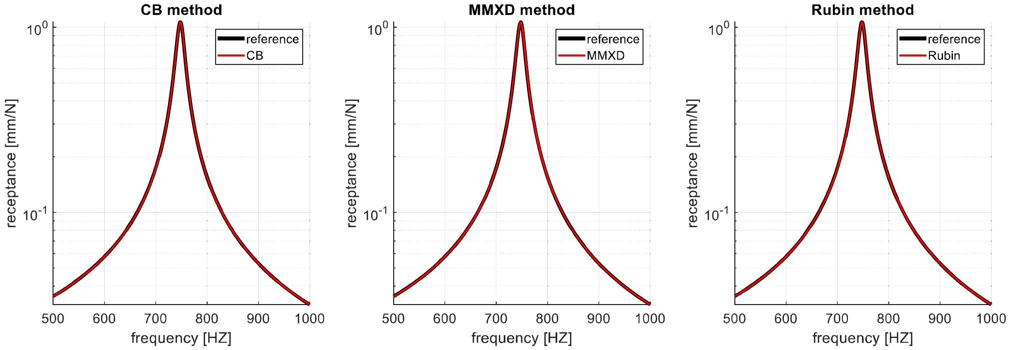

Figure 4.11. Receptance comparison for the case with zero mistuning

For the following sections, different mistuning patterns will be applied to the blades, and the applicability of the reduction methods is going to be investigated.

4.3.2 Mistuning Pattern #1

As for the case with zero mistuning, the investigation starts with comparing natural frequencies. Figure 4.11 illustrates the natural frequencies up to 800 provided by the three different reduction methods.

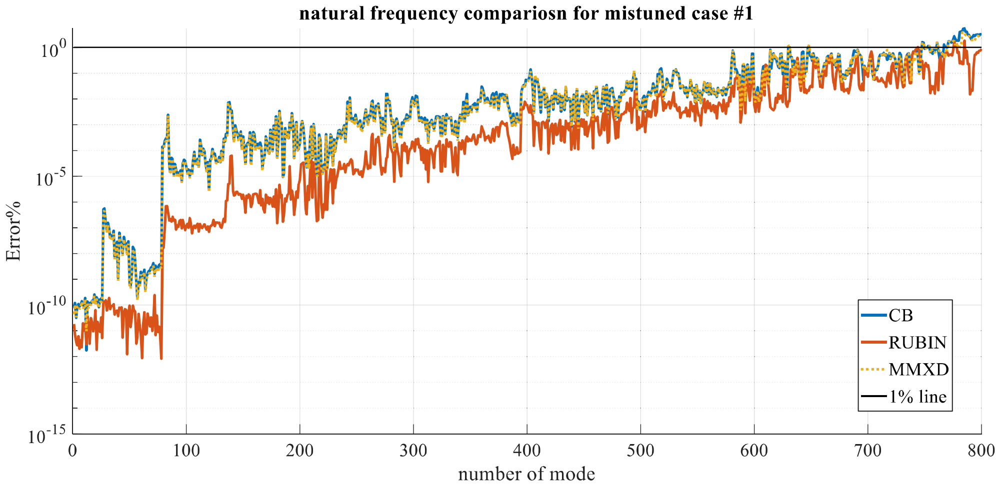

Figure 4.12. Natural frequency comparison for the case with mistuning pattern #1

At first glance, it can be concluded that all methods can accurately predict the natural frequencies of the mistuned bladed disk with perfect accuracy. However, the error criteria from the Rubin method remain under the two other methods for almost all of the natural frequencies. Another critical point is that the error criteria follow a steady increase along with the natural frequency number in contrast to the case with zero mistuning. The latter is customary for typical systems with no cyclic symmetry, suggesting that mistuning successfully has destroyed the cyclic symmetry.

Subsequently, the mode shape comparison by means of MAC number is carried out. For this case, in line with the frequency error behavior, a steady decrease in the mac number along mode shape number is anticipated.

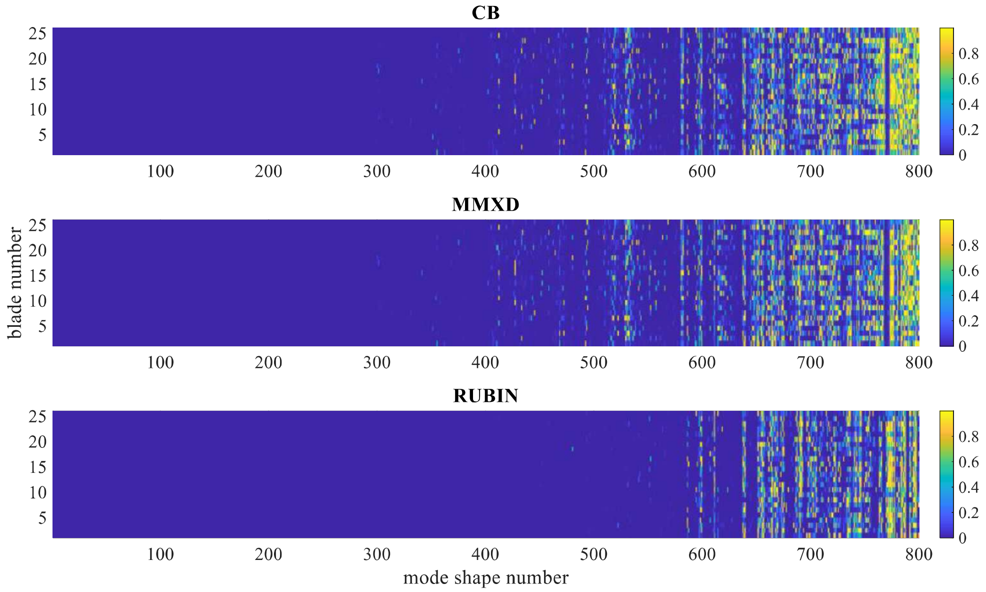

Figure 4.13. Mode shape comparison for the case with mistuning pattern #1

Table 4.8 MAC number for the mistuning pattern #1

Method	0.99	0.95	0.9	0.75	0.5
CB	581	710	767	767	767
MMXD	581	689	773	774	790
RUBIN	654	664	771	774	800

The results shown in the figure above exactly match the anticipation made. As it is shown, the fluctuation of the MAC numbers is gone. Apart from this, the Rubin method outperforms others again in terms of mode shape accuracy.

Finally, receptance values are derived. Figure 4.13 illustrates the results for the receptance matrices. It can be seen that for the mistuned case also, there are no visual differences between the reduced-order model results and reference values.

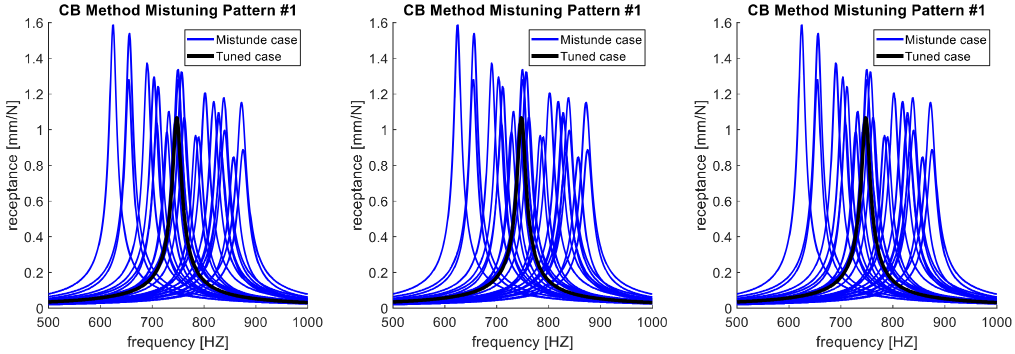

Figure 4.14. Receptance comparison for the case with mistuning pattern #1

4.3.3 Mistuning Pattern #2

Finally, another mistuning pattern is applied to the blades. This time a random mistuning with normal distribution is considered. A comprehensive description of each mistuning pattern is given in chapter two.

In line with the previous cases, first natural frequencies are compared in Figure 4.14. There is not a significant difference between this case and the previous one. Again, all reduction methods based on CMS can successfully determine the system's natural frequencies.

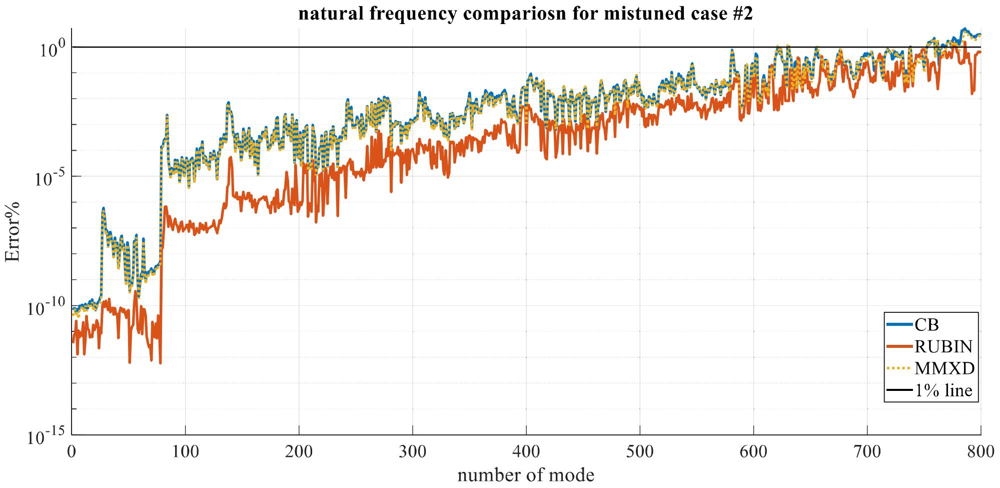

Figure 4.15. Natural frequency comparison for the case with mistuning pattern #2

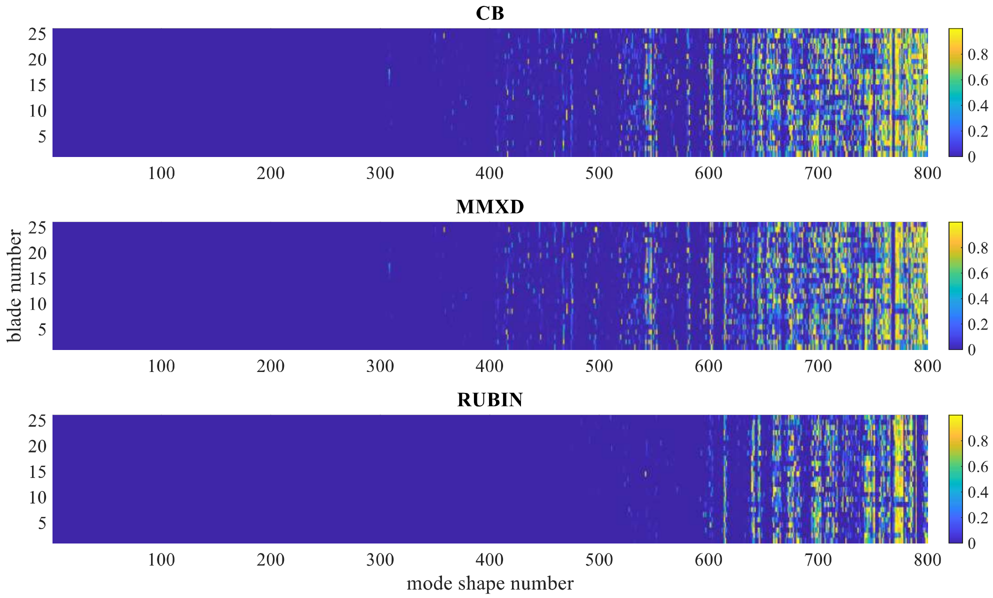

Figure 4.16. Mode shape comparison for the case with mistuning pattern #2

The MAC number and receptance coefficient results are similar to the previous case and are illustrated below. These results, along with the ones obtained from the previous cases, testify to the validity of the reduced-order model.

Table 4.9 MAC number for the mistuning pattern #2

Method	0.99	0.95	0.9	0.75	0.5
CB	547	761	766	766	800
MMXD	547	561	562	784	792
RUBIN	639	751	770	800	800

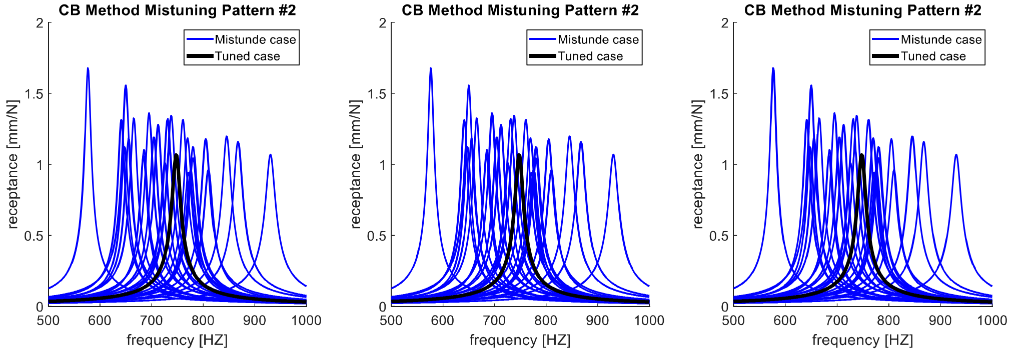

Figure 4.17. Receptance coefficient for the case with mistuning pattern #2

From the obtained results, it can be concluded that the third approach is a valid reduced-order model for the system. For the disk segment, there were three options, as described at the beginning of this chapter. The results in this section suggest that the Rubin method outperforms others for the disk substructure. One reason for this behavior could be the large disk to disk interface. Since many DOFs are included in the disk to disk interface, fixing them results in inaccurate responses.

The MMXD method has been shown to provide superior results for the blade sector. Thus, the third approach was coupled with a reduced blade system derived from the MMXD method.

4.4 Monte-Carlo Simulation

An efficient and accurate model for the mistuning bladed disk case is derived in the previous section. In this section, the reduced-order model is implemented in the Monte-Carlo simulation in order to identify the mistuning pattern and its effect on the deviation of the natural frequencies and receptance values.

It should be noted that, since this analysis is only conducted to see the random nature of the mistuning phenomenon, only two nodes (6 DOFs) from the shroud surface are included in the final DOFs of the reduced model. Moreover, five modes from the blade substructure and two modes from the disk substructure are added to the reduction basis. This allows us to predict the results of the mistuned system up to 52 natural frequencies. Simultaneously, the size of the matrices is further reduced to enhance the computational process.

For a comprehensive statistical evaluation, two different patterns of the random numbers are considered. First, random numbers with uniform distribution with various deviation ranges. Second, random numbers with normal distribution and different standard deviations.

For each case of mistuning, a set of 26 random numbers (for each blade) are generated. Subsequently, mistuning is projected onto the blades according to the generated random numbers. A modal analysis is conducted to obtain the natural frequencies and the receptance values for the interested frequency range. The procedure is repeated for 100 different mistuning patterns to derive the statistical data.

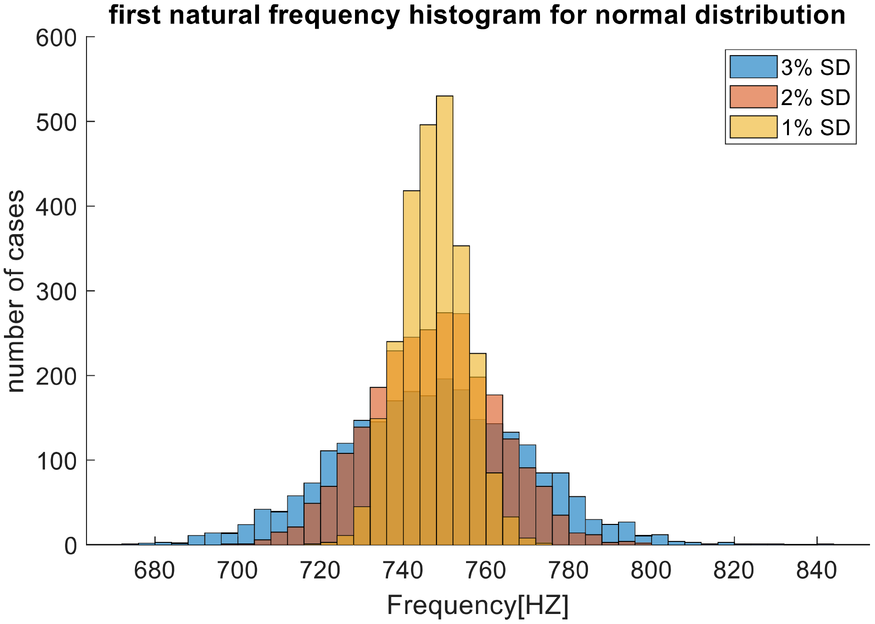

Figure 4.18. Distribution of the first natural frequency of mistuned system with normal distribution

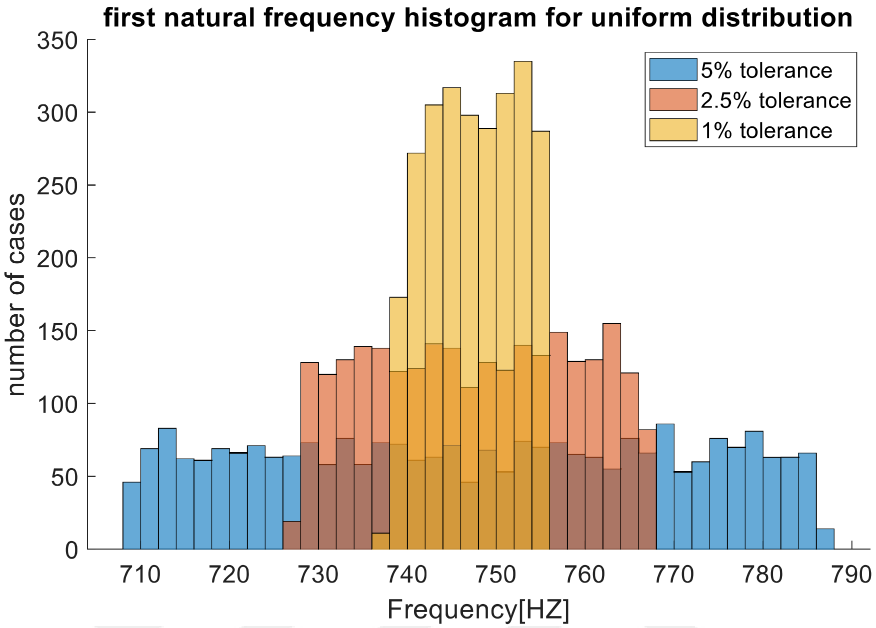

Figure 4.19. Distribution of the first natural frequency of mistuned system with uniform distribution

For the first step, a histogram plot of the first natural frequency of the mistuned system is provided. As shown in Figure 4.17., the normal distribution of the mistuning pattern is also projected on the first natural frequencies of the mistuned case. The distribution pattern is also projected on the first natural frequency as expected for the uniform distribution Figure(4.18.).

It should be noted that the first 26 natural frequencies of the mistuned case indeed pertain to the first natural frequency of the tuned systems since there is no longer symmetry in the system. Therefore there are 2600 values available for the natural frequencies.

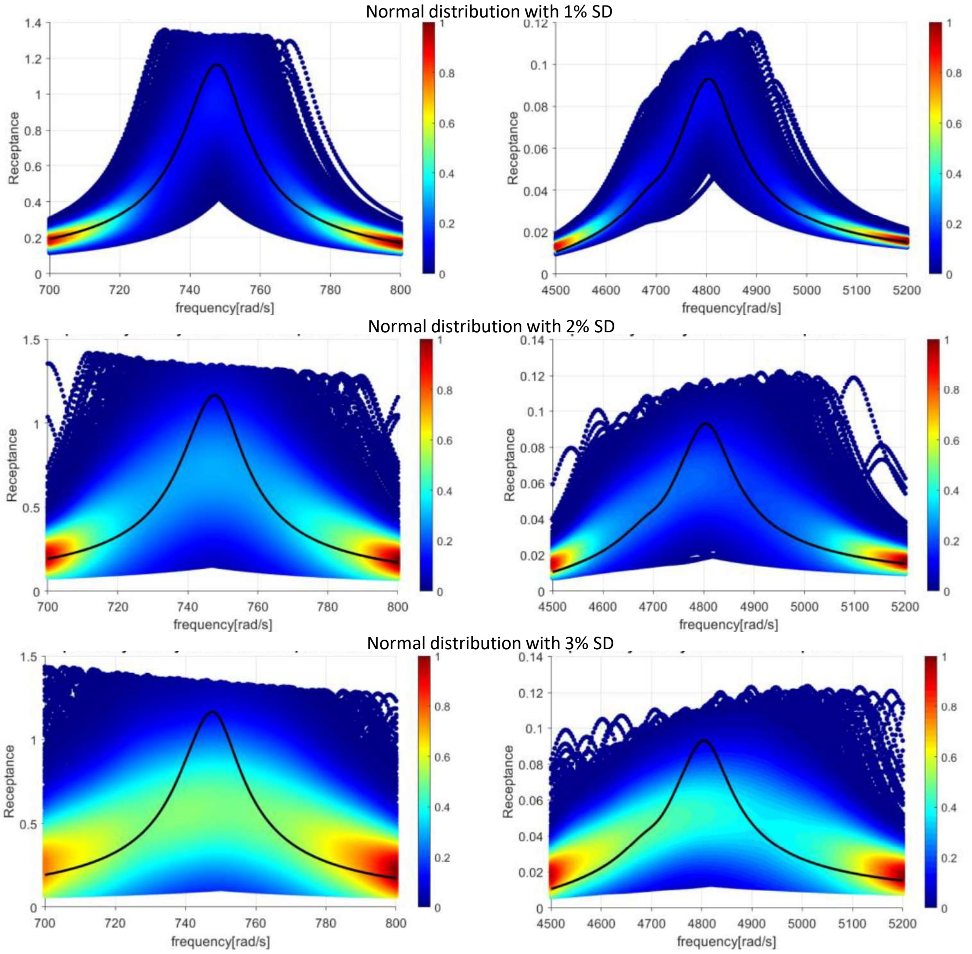

Figure 4.20. Probability distribution of the receptance values for mistuning pattern with normal distribution

For the next step, the Mote-Carlo simulation is implemented to acquire a statistical sense of the receptance values around the first and the second tuned natural frequencies. To this end, the receptance value points are scattered on a plane with its x-axis containing the frequencies and its y-axis indicating the receptance values. Subsequently, a probability density function is fitted for the receptance values for each frequency step. Finally, a contour plot is derived, illustrating the concentration of the receptance values at specific points.

Uniform distribution with 1% tolerance

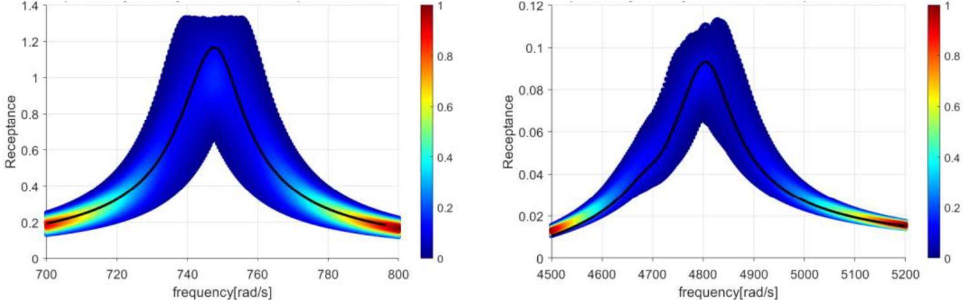

Uniform distribution with 2.5% tolerance

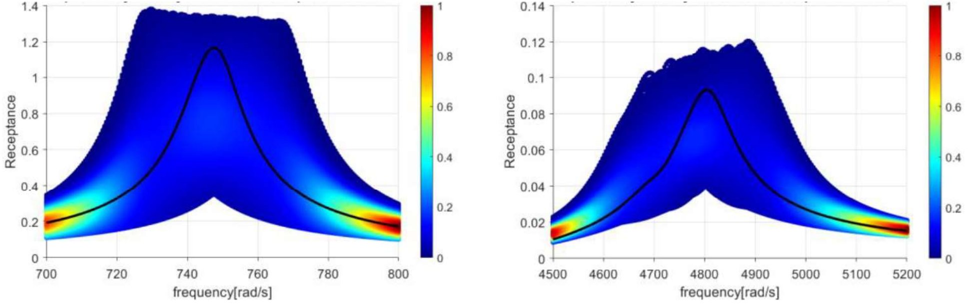

Uniform distribution with 5% tolerance

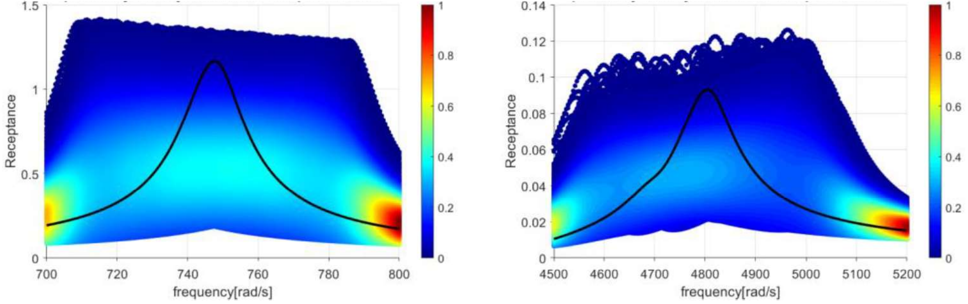

Figure 4.21. Probability distribution of the receptance values for mistuning pattern with uniform distribution

In order to better observe the mistuning phenomena, the receptance values around the first and second natural frequencies are plotted separately to avoid the gap between the frequencies.

From Figures 4.19 and 4.20, it can be concluded that by increasing the SD values or the deviation range, the receptance values widely spread around the tuned case. The receptance points converge toward the tuned case solution by decreasing SD or tolerance. Moreover, it can be concluded from the plots that the vibrational behavior of the system around its tuned natural frequencies is more prone to perturbation with respect to mistuning. Conversely, the system tends to vibrate close to the tuned vibration pattern in the frequency ranges away from the natural frequencies. Nevertheless, the range of deviation from the tuned case directly correlates with the values of SD or tolerance.

CHAPTER 5

CONCLUSION AND FUTURE WORK

In this study, reduced-order modeling for bladed disk systems is investigated. An outline for each chapter is presented below.

Starting from chapter one, an introduction to the vibration analysis of bladed disk systems and a comprehensive literature survey on different approaches to tackle the problem of reduced-order modeling for both tuned and mistuned bladed disk systems are presented.

Chapter two is dedicated to describing the different methodologies required for reduction procedures together with an instruction for mistuning modeling. First of all, the famous cyclic symmetry property is formulated. Both real and imaginary formulation of the cyclic symmetry is given together with a mode shape interpretation for both formulations. Afterward, the reduction techniques based on Component Mode Synthesis are described. Almost all of the conventional reduction techniques are formulated in this section, namely, Craig-Bampton, Rubin, Dual Craig-Bampton, and mixed interface. A new reduction setup is proposed for the specific geometry of bladed disk systems by comparing the reduction technique. The method is addressed as Modified Mixed Interface Method (MMXD). Moreover, a new interface reduction procedure is derived. The method extends the conventional interface reduction called “modal reduction of interface DOFs,” which considers a more general case where there are DOFs other than interface in the matrices. Finally, the chapter includes mistuning modeling, which describes how mistuning is projected on the blade sectors.

The next chapter mainly discussed the finite element model and the case studies. First, the properties of the finite element model for the bladed disk are given. Subsequently, a reduced-order model strategy for tuned bladed disk assemblies is formulated. It is shown that the reduction procedure is confined to the reduction of the fundamental sector for the tuned bladed disk system since the expansion of the fundamental sector to the overall bladed disk assembly is carried out using the cyclic symmetry property. All of the CMS reduction methods are implemented to reduce the size of the fundamental sector, allowing to conduct a comprehensive comparison study. The following section is concentrated on the mistuned bladed disk assembly. For the specific case of mistuning where cyclic symmetry is no longer valid, the vibration analysis cost increases significantly; consequently, a much more sophisticated reduction procedure is required. The reduction of blades is analogous to the tuned case since there is no direct coupling between the blades. However, for the disk assembly, a combination of the cyclic symmetry property and CMS methods are considered to build an efficient reduction basis for the disk segment.

Finally, results from modal analysis of both tuned and mistuned systems are presented in chapter 4. In addition, discussion and analytical intrepretation of the results are provided. For the tuned bladed disk system, an assessment is made of the most efficient reduction technique. Since the focal point of this research is to determine the extent of contribution of each substructure to the final vibration state of the assembly, a different number of modes are considered in the reduction basis. The following conclusions can be made from the comparative study of the tuned bladed disk system:

- The type of vibration modes (whether they are derived with fixed or free interfaces), severely affects the final accuracy of a reduction technique.
- Although the contribution of the disk vibration to the overall vibration of the system near its fundamental frequency is negligible; however, as soon as the 6^{th} or higher natural frequencies are reached, the effect of adding the vibration modes of the disk sector to the reduction basis can be clearly seen.
- The free interface methods demonstrate outstanding accuracy; however, in the case of existing rigid body motion, the computational cost is significantly more.

Based on the observation from this part, a modified mixed interface method is proposed—this new reduction setup consists of the conventional Rubin and Craig-Bampton methods. The proposed method provides a possibility to include such vibration modes from both blade and disk sectors that can closely resemble the overall vibration pattern of the system and therefore build a more efficient reduction basis. It should be noted that including vibration modes into the reduction basis is the most straightforward way to increase the accuracy of the method. Thus, it is very important to consider such vibration modes that are better compatible with the physique of the geometry. The comparison studies showed that the Modified Mixed Method (proposed in this study) provides accurate results with relatively less computational effort. In particular, the mode shapes and frequency response functions on the shrouds DOFs which are of immense importance for nonlinear contact elements, are anticipated better by the proposed method.

For the mistuned case, the blade segment is reduced by the MMXD method since it has been shown that the mode shapes considered by the MMXD method better resemble the vibration patted of the entire assembly. However, for the disk segment, three different reduction approach is proposed. It is shown that only one of the approaches is practically applicable for the reduction of the system, namely the third approach. This is mostly due to the fact that very large matrices are required when cyclic symmetry is no longer valid, and mistuning is taken into consideration. Consequently, more advanced reduction methodologies are needed to tackle the high computational cost. The third approach includes cyclic symmetry, CMS reduction, and a new interface reduction, all of which enable it to reduce the disk segment efficiently. The following are the most notable conclusions from the mistuned case study:

- A proper combination of cyclic symmetry, CMS methods, and interface reduction can provide a very efficient reduced-order model that can reduce the computational time drastically while providing modal information with very high accuracy.

- For the disk sector, it is shown a prior that blade to disk interface is better to be reduced using free interface methods. In the mistuned case study, it turns out that the disk to disk interface is also better to be described with attachment modes. This conclusion came from the observation that the Rubin method performs better for the disk sector.
- The reduction basis provided by the methods given can bring accurate results regardless of the mistuning type.

5.1 Future Work

In this thesis work, reduction methods based on CMS and their applicability to tuned and mistuned systems are tested. Here are some future works which can be done:

- Rotodynamic effects, namely spin softening, stress stiffening, and Coriolis effect, can be included in the vibration analysis of the bladed disk system. Moreover, the vibration of the bladed disk mounted on a shaft can be considered for a more realistic vibration investigation.
- The most time-consuming part of the vibration analysis is solving the generalized eigenvalue problem. A complementary part for the reduction measure is given in this thesis could be a more efficient algorithm to calculate the eigenvalue problem.
- The modal results on the shroud surfaces provided by the reduction methods given in this thesis can be fed into a nonlinear solver in order to account for the nonlinearity of the contact surfaces.

REFERENCES

[1] D. J. Ewins, “Vibration modes of mistuned bladed disks,” *Journal of Engineering for Gas Turbines and Power*, vol. 98, no. 3, pp. 349–355, 1976, doi: 10.1115/1.3446180.

[2] C. M. P. Bladh R., “Component-mode-based reduced order modeling techniques for mistuned bladed disks-Part 1: Theoretical models,” *Journal of Engineering for Gas Turbines and Power*, vol. 123, no. 1, pp. 89–99, 2001, doi: 10.1115/1.1338947.

[3] E. P. Petrov, “A high-accuracy model reduction for analysis of nonlinear vibrations in structures with contact interfaces,” *Journal of Engineering for Gas Turbines and Power*, vol. 133, no. 10, pp. 1–10, 2011, doi: 10.1115/1.4002810.

[4] R. R. Craig and A. J. Kurdila, “Fundamentals of Structural Dynamics”.

[5] D. De Klerk, D. J. Rixen, and S. N. Voormeeren, “General framework for dynamic substructuring: History, review, and classification of techniques,” *AIAA Journal*, vol. 46, no. 5, pp. 1169–1181, 2008, doi: 10.2514/1.33274.

[6] R. Craig and M. Bampton, “Coupling of Substructures for Dynamic Analyses To cite this version : HAL Id : hal-01537654 Coupling of Substructures for Dynamic Analyses,” *AIAA Journal*, vol. 6, no. 7, pp. 1313–1319, 1968.

[7] S. Rubin, “Improved component-mode representation for structural dynamic analysis,” *AIAA Journal*, vol. 13, no. 8, pp. 995–1006, 1975, doi: 10.2514/3.60497.

[8] R. R. Craig, “Coupling of substructures for dynamic analyses: An overview,” *Collection of Technical Papers - AIAA/ASME/ASCE/AHS/ASC*

Structures, Structural Dynamics and Materials Conference, vol. 5, pp. 3–14, 2000, doi: 10.2514/6.2000-1573.

[9] W. C. Hurty, “Dynamic analysis of structural systems using component modes,” *AIAA Journal*, vol. 3, no. 4, pp. 678–685, 1965, doi: 10.2514/3.2947.

[10] R. Craig and M. Bampton, “Coupling of Substructures for Dynamic Analyses,” *AIAA Journal, American Institute of Aeronautics and Astronautics*, vol. 6, no. 7, pp. 1313–1319, 1968, doi: 10.2514/3.4741ï.

[11] R. H. MacNeal, “A hybrid method of component mode synthesis,” *Computers & Structures*, vol. 1, no. 4, pp. 581–601, Dec. 1971, doi: 10.1016/0045-7949(71)90031-9.

[12] R. M. Hintz, “Analytical methods in component modal synthesis,” *AIAA Journal*, vol. 13, no. 8, pp. 1007–1016, 1975, doi: 10.2514/3.60498.

[13] P. Seshu, “Substructuring and component mode synthesis,” *Shock and Vibration*, vol. 4, no. 3, pp. 199–210, 1997, doi: 10.1155/1997/147513.

[14] H. Irretier and K. J. Schmidt, “MISTUNED BLADED DISKS - DYNAMICAL BEHAVIOUR AND COMPUTATION.,” *Energia Elettrica*, vol. 59, no. 10, pp. 215–226, 1982.

[15] S.-B. Chun and C.-W. Lee, “Vibration analysis of shaft-bladed disk system by using substructure synthesis and assumed modes method,” *Journal of Sound and Vibration*, vol. 189, no. 5, pp. 587–608, 1996, doi: 10.1006/jsvi.1996.0038.

[16] R. Bladh, M. P. Castanier, and C. Pierre, “Reduced order modeling and vibration analysis of mistuned bladed disk assemblies with shrouds,” *Journal of Engineering for Gas Turbines and Power*, vol. 121, no. 3, pp. 515–522, 1999, doi: 10.1115/1.2818503.

[17] C. M. P. Bladh R., “Component-mode-based reduced order modeling techniques for mistuned bladed disks-Part 1: Theoretical models,” *Journal of Engineering for Gas Turbines and Power*, vol. 123, no. 1, pp. 89–99, 2001, doi: 10.1115/1.1338947.

[18] C. M. P. Bladh R., “Component-mode-based reduced order modeling techniques for mistuned bladed disks-Part II: Application,” *Journal of Engineering for Gas Turbines and Power*, vol. 123, no. 1, pp. 100–108, 2001, doi: 10.1115/1.1338948.

[19] F. Mashayekhi, S. Zucca, and A. S. Nobari, “Evaluation of free interface-based reduction techniques for nonlinear forced response analysis of shrouded blades,” *Proceedings of the Institution of Mechanical Engineers, Part C: Journal of Mechanical Engineering Science*, vol. 233, no. 23–24, pp. 7459–7475, 2019, doi: 10.1177/0954406219872523.

[20] F. Mashayekhi, S. Zucca, and A. S. Nobari, “A Comparison of Two Reduction Techniques for Forced Response of Shrouded Blades with Contact Interfaces,” vol. 4, pp. 79–88, 2018, doi: 10.1007/978-3-319-74654-8_7.

[21] F. Mashayekhi, A. S. Nobari, and S. Zucca, “Hybrid reduction of mistuned bladed disks for nonlinear forced response analysis with dry friction,” *International Journal of Non-Linear Mechanics*, vol. 116, no. June, pp. 73–84, 2019, doi: 10.1016/j.ijnonlinmec.2019.06.001.

[22] S. Mehrdad Pourkiaee and S. Zucca, “A Reduced Order Model for Nonlinear Dynamics of Mistuned Bladed Disks with Shroud Friction Contacts,” *Journal of Engineering for Gas Turbines and Power*, vol. 141, no. 1, 2019, doi: 10.1115/1.4041653.

[23] S. M. Pourkiaee and S. Zucca, “Mixed-Boundary Component Mode Substitution for Nonlinear Dynamics of Mistuned Shrouded Bladed Disks,” *AIAA Journal*, vol. 58, no. 1, pp. 402–414, 2020, doi: 10.2514/1.j058561.

[24] S. M. Pourkiaee, S. Zucca, and R. G. Parker, “Relative cyclic component mode synthesis: A reduced order modeling approach for mistuned bladed disks with friction interfaces,” *Mechanical Systems and Signal Processing*, vol. 163, no. February 2021, 2021, doi: 10.1016/j.ymssp.2021.108197.

[25] W. A. Benfield and R. F. Hruda, “Vibration analysis of structures by component mode substitution,” *AIAA Journal*, vol. 9, no. 7, pp. 1255–1261, 1971, doi: 10.2514/3.49936.

[26] J. Yuan, C. Schwingshackl, C. Wong, and L. Salles, “On an improved adaptive reduced-order model for the computation of steady-state vibrations in large-scale non-conservative systems with friction joints,” *Nonlinear Dynamics*, vol. 103, no. 4, pp. 3283–3300, 2021, doi: 10.1007/s11071-020-05890-2.

[27] S. Quaegebeur, B. Chouvion, and F. Thouverez, “Nonlinear cyclic reduction for the analysis of mistuned cyclic systems,” *Journal of Sound and Vibration*, vol. 499, 2021, doi: 10.1016/j.jsv.2021.116002.

[28] S. Quaegebeur, B. Chouvion, F. Thouverez, and L. Berthe, “On a New Nonlinear Reduced-Order Model for Capturing Internal Resonances in Intentionally Mistuned Cyclic Structures,” *Journal of Engineering for Gas Turbines and Power*, vol. 143, no. 2, 2021, doi: 10.1115/1.4049138.

[29] “cyclic symmetry MSC-NASTRAN”.

[30] G. Jenovencio and D. J. Rixen, “A DUAL FORMULATION OF CYCLIC SYMMETRY: APPLICATION IN FREE VIBRATION ANALYSIS.”

[31] C. L. Fortescue, “METHOD OF SYMMETRICAL CO-ORDINATES APPLIED TO THE SOLUTION OF POLYPHASE NETWORKS,” 1918.

[32] D. Thomas, D. Thomas Dynamics, and D. L. Thomas, “of rotationally periodic structures,” *International Journal for Numerical Methods in*

Engineering, vol. 14, no. 1, pp. 81–102, 1979, doi: 10.1002/nme.1620140107ï.

[33] B. J. Olson, S. W. Shaw, C. Shi, C. Pierre, and R. G. Parker, “Circulant matrices and their application to vibration analysis,” *Applied Mechanics Reviews*, vol. 66, no. 4, 2014, doi: 10.1115/1.4027722.

[34] E. P. Petrov, “A method for use of cyclic symmetry properties in analysis of nonlinear multiharmonic vibrations of bladed disks,” *Journal of Turbomachinery*, vol. 126, no. 1, pp. 175–183, Jan. 2004, doi: 10.1115/1.1644558.

[35] “(Pure & Applied Mathematics) Philip J. Davis - Circulant Matrices-John Wiley & Sons Inc (1979)”.

[36] R. J. Guyan, “Reduction of stiffness and mass matrices,” *AIAA Journal*, vol. 3, no. 2, p. 380, 1965, doi: 10.2514/3.2874.

[37] A. Y. Leung, “An accurate method of dynamic condensation in structural analysis,” *International Journal for Numerical Methods in Engineering*, vol. 12, no. 11, pp. 1705–1715, Jan. 1978, doi: 10.1002/NME.1620121108.

[38] S. N. Voormeeren, *Dynamic substructuring methodologies for integrated dynamic analysis of wind turbines*, no. november. 2012.

[39] D. J. Rixen, “A dual Craig-Bampton method for dynamic substructuring,” *Journal of Computational and Applied Mathematics*, vol. 168, no. 1–2, pp. 383–391, 2004, doi: 10.1016/j.cam.2003.12.014.

[40] M. S. Allen, D. Rixen, M. van der Seijs, P. Tiso, T. Abrahamsson, and R. L. Mayes, *Substructuring in Engineering Dynamics*, vol. 594. 2020.

[41] A. Majed and E. E. Henkel, “Improved Method of Mixed-Boundary Component-Mode,” vol. 42, no. 5, 2005.

[42] W. Witteveen and H. Irschik, “Efficient Mode Based Computational Approach for Jointed Structures: Joint Interface Modes,” *https://doi.org/10.2514/1.38436*, vol. 47, no. 1, pp. 252–263, May 2012, doi: 10.2514/1.38436.

[43] M. Junge, D. Brunner, J. Becker, and L. Gaul, “Interface-reduction for the Craig-Bampton and Rubin method applied to FE-BE coupling with a large fluid-structure interface,” *International Journal for Numerical Methods in Engineering*, vol. 77, no. 12, pp. 1731–1752, 2009, doi: 10.1002/NME.2474.

[44] S. N. Voormeeren, *Dynamic substructuring methodologies for integrated dynamic analysis of wind turbines*, no. november. 2012.

[45] D. M. Tran, “Component mode synthesis methods using partial interface modes: Application to tuned and mistuned structures with cyclic symmetry,” *Computers and Structures*, vol. 87, no. 17–18, pp. 1141–1153, 2009, doi: 10.1016/j.compstruc.2009.04.009.

[46] D. M. Tran, “Component mode synthesis methods using interface modes. Application to structures with cyclic symmetry,” *Computers & Structures*, vol. 79, no. 2, pp. 209–222, Jan. 2001, doi: 10.1016/S0045-7949(00)00121-8.

[47] D. Krattiger *et al.*, “Interface reduction for Hurty/Craig-Bampton substructured models: Review and improvements,” *Mechanical Systems and Signal Processing*, vol. 114, pp. 579–603, 2019, doi: 10.1016/j.ymssp.2018.05.031.

[48] E. Balmès, “Use of Generalized Interface Degrees of Freedom in Component Mode Synthesis.”

[49] R. R. Craig and Z. Ni, “Component mode synthesis for model order reduction of nonclassicallydamped systems,” *https://doi.org/10.2514/3.20446*, vol. 12, no. 4, pp. 577–584, May 2012, doi: 10.2514/3.20446.

[50] D. de Klerk, D. J. Rixen, and S. N. Voormeeren, “General framework for dynamic substructuring: History, review, and classification of techniques,” *AIAA Journal*, vol. 46, no. 5, pp. 1169–1181, 2008, doi: 10.2514/1.33274.

[51] M. P. Castanier and C. Pierre, “Modeling and analysis of mistuned bladed disk vibration: Status and emerging directions,” *Journal of Propulsion and Power*, vol. 22, no. 2, pp. 384–396, 2006, doi: 10.2514/1.16345.

[52] D. M. Feiner and J. H. Griffin, “Mistuning identification of bladed disks using a fundamental mistuning model - Part I: Theory,” *Journal of Turbomachinery*, vol. 126, no. 1, pp. 150–158, 2004, doi: 10.1115/1.1643913.

[53] D. M. Feiner and J. H. Griffin, “Mistuning identification of bladed disks using a fundamental mistuning model - Part II: Application,” *Journal of Turbomachinery*, vol. 126, no. 1, pp. 159–165, 2004, doi: 10.1115/1.1643914.

[54] J. Yuan, F. Scarpa, G. Allegri, B. Titurus, S. Patsias, and R. Rajasekaran, “Efficient computational techniques for mistuning analysis of bladed discs: A review,” *Mechanical Systems and Signal Processing*, vol. 87. Academic Press, pp. 71–90, Mar. 15, 2017. doi: 10.1016/j.ymssp.2016.09.041.

[55] B. Salhi, J. Lardiès, M. Berthillier, P. Voinis, and C. Bodel, “Modal parameter identification of mistuned bladed disks using tip timing data,” *Journal of Sound and Vibration*, vol. 314, no. 3–5, pp. 885–906, 2008, doi: 10.1016/j.jsv.2008.01.050.

[56] W. Tang, S. Baek, and B. I. Epureanu, “Reduced-Order Models for Blisks with Small and Large Mistuning and Friction Dampers,” *Journal of Engineering for Gas Turbines and Power*, vol. 139, no. 1, 2017, doi: 10.1115/1.4034212.

[57] D. M. Feiner and J. H. Griffin, "A fundamental model of mistuning for a single family of modes," *Journal of Turbomachinery*, vol. 124, no. 4, pp. 597–605, Oct. 2002, doi: 10.1115/1.1508384.

[58] S.-H. Lim, R. Bladh, M. P. Castanier, and C. Pierre, "Compact, generalized component mode mistuning representation for modeling bladed disk vibration," *AIAA Journal*, vol. 45, no. 9, pp. 2285–2298, 2007, doi: 10.2514/1.13172.

[59] A. C. Madden, M. P. Castanier, and B. I. Epureanu, "Reduced-order model construction procedure for robust mistuning identification of blisks," *AIAA Journal*, vol. 46, no. 11, pp. 2890–2898, 2008, doi: 10.2514/1.37314.

[60] D. J. Ewins, "VIBRATION CHARACTERISTICS OF BLADED DISC ASSEMBLIES."

[61] S.-T. Wei, G. Research, and A. C. Pierre, "Localization Phenomena in Mistimed Assemblies with Cyclic Symmetry Part II: Forced Vibrations," 1988. [Online]. Available: http://vibrationacoustics.asmedigitalcollection.asme.org/

[62] S.-T. Wei, G. Research, and A. C. Pierre, "Localization Phenomena in Mistimed Assemblies with Cyclic Symmetry Part I: Free Vibrations," 1988. [Online]. Available: http://vibrationacoustics.asmedigitalcollection.asme.org/